Formation of highly Zn-enriched sulfide scale at a deep-sea artificial hydrothermal vent, Iheya-North Knoll, Okinawa Trough

Nozaki, Tatsuo ; Nagase, Toshiro ; Torimoto, Junji ; Takaya, Yutaro ; Ishibashi, Jun-ichiro ; Shimada, Kazuhiko ; Watanabe, Masayuki ;…

(Citation)
Miner Deposita,56:975-990

(Issue Date)
2020-10-29

(Resource Type)
journal article

(Version)
Accepted Manuscript

Formation of highly Zn-enriched sulfide scale at a deep-sea artificial hydrothermal vent, Iheya-North Knoll, Okinawa Trough

Tatsuo Nozaki[1,2,3,4], Toshiro Nagase[5], Junji Torimoto[6], Yutaro Takaya[7,1,4], Jun-ichiro Ishibashi[8], Kazuhiko Shimada[8], Masayuki Watanabe[1], Yuka Masaki[9], Koichi Iijima[1], Kazuya Kitada[10], Masafumi Saitoh[11], Takahiro Yokoyama[12], Keita Akiyama[12], Noriaki Sakurai[12], Tomokazu Saruhashi[12], Masanori Kyo[12], Hidenori Kumagai[1] and Lena Maeda[12]

[1]Submarine Resources Research Center, Research Institute for Marine Resources Utilization, Japan Agency for Marine-Earth Science and Technology (JAMSTEC), 2-15 Natsushima-cho, Yokosuka, Kanagawa 237-0061, Japan

[2]Frontier Research Center for Energy and Resources (FRCER), The University of Tokyo, 7-3-1 Hongo, Bunkyo-ku, Tokyo 113-8656, Japan

[3]Department of Planetology, Kobe University, 1-1 Rokkodai-cho, Nada-ku, Kobe, Hyogo 657-8501, Japan

[4]Ocean Resources Research Center for Next Generation, Chiba Institute of Technology, 2-17-1 Tsudanuma, Narashino, Chiba 275-0016, Japan

[5]The Tohoku University Museum, The Center for Academic Resources and Archives,

Tohoku University, 6-3 Aoba, Aramaki, Aoba-ku, Sendai, Miyagi 980-8578, Japan

[6]Project Team for Development of New-Generation Research Protocol for Submarine Resources, Japan Agency for Marine-Earth Science and Technology (JAMSTEC), 2-15 Natsushima-cho, Yokosuka, Kanagawa 237-0061, Japan

[7]Faculty of Science and Engineering, Waseda University, 3-4-1 Okubo, Shinjuku-ku, Tokyo 169-8555, Japan

[8]Department of Earth and Planetary Sciences, Faculty of Science, Kyushu University, 744 Motooka, Nishi-ku, Fukuoka 819-0395, Japan

[9]Cosmos Shoji Co., Ltd., 2-11 Kanda Nishiki-cho, Chiyoda-ku, Tokyo 101-0054, Japan

[10]Institute for Extra-cutting-edge Science and Technology Avant-garde Research (X-star), Japan Agency for Marine-Earth Science and Technology (JAMSTEC), 2-15 Natsushima-cho, Yokosuka, Kanagawa 237-0061, Japan

[11]Institut des sciences de la Terre, Université de Lausanne, Géopolis, 1015 Lausanne, Switzerland

[12]Institute for Marine-Earth Exploration and Engineering, Japan Agency for Marine-Earth Science and Technology (JAMSTEC), 2-15 Natsushima-cho, Yokosuka, Kanagawa 237-0061, Japan

E-mail address: Tatsuo Nozaki, nozaki@jamstec.go.jp

Abstract

Artificial hydrothermal vents, created by boreholes that discharge hydrothermal fluids and useful for observing secular changes in mineral precipitates and the chemical compositions of hydrothermal fluids, are periodically cleaned of scale deposits. Here, we report petrographic and geochemical features of hydrothermal scale with a concentric structure and extreme enrichment in Zn, recovered as an intact plug from an artificial hydrothermal vent pipe in the Okinawa Trough. The scale consists of sphalerite with accessory galena and chalcopyrite, and minor cotunnite ($PbCl_2$), barite, an unidentified Zn-sulfate, and Bi-rich minerals. It comprises at least five concentric layers alternating between thin, reddish-brown porous layers composed of relatively Fe-rich sphalerite accompanied by galena and chalcopyrite, and coarse-grained, dark gray layers dominated by relatively Fe-poor sphalerite. Cotunnite occurs only in the innermost reddish-brown layer, and barite occurs only in the uppermost and innermost layers. The scale is composed of >50 wt% Zn, several wt% Fe and Pb, and <1 wt% Cu, Mn, and Cd, a composition consistent with the solubility of Zn and Cu in a hydrothermal fluid at 304–311°C and pH 4.7–5.0. We suggest that the concentric layers are related to periodic scale-removal operations through which (1) mostly clogged pipe conditions and weak

hydrothermal discharge alternate with (2) fully open pipe conditions and vigorous hydrothermal discharge, thus affecting sulfur fugacity and [Cl^-] and [SO_4^{2-}] activities in the hydrothermal fluid and leading to the formation of concentric layers of precipitated minerals.

Keywords: Hydrothermal scale, deep-sea artificial hydrothermal vent, Iheya-North Knoll, Okinawa Trough, seafloor massive sulfide (SMS) deposits, Hole C0014G

INTRODUCTION

Volcanogenic massive sulfide (VMS) deposits, found worldwide in strata of various geological ages, are major Cu-Pb-Zn±Au±Ag resources (Franklin et al. 2005; Mosier et al. 2009; Nozaki et al. 2013; Piercey 2011). Seafloor massive sulfide (SMS) deposits, the modern natural analogue of VMS deposits on land, are being vigorously explored as potential producers of these base and precious metals (e.g., Beaulieu et al. 2015; Hannington et al. 2011). In 2010, drilling during IODP Expedition 331 at Iheya-North Knoll in the Okinawa Trough, East China Sea, induced the formation of "deep-sea artificial hydrothermal vents" (at Holes C0013E, C0014G, C0016A, and C0016B), i.e., drill holes in which hydrothermal fluid was allowed to flow freely (Figs. 1 and 2) (Takai

et al. 2011, 2012). At Hole C0016A, the uncased hole gave rise to a sulfide chimney that was observed to grow by 7 m per year during several dive surveys made by a remotely operated vehicle (ROV) (Kawagucci et al. 2013).

Because such chimneys formed from artificial hydrothermal vents have Cu, Pb, and Zn contents very similar to those of high-grade Kuroko-type VMS deposits (Nozaki et al. 2016), in 2016 we started a research project on the formation (cultivation) of Kuroko-type ore that included an *in-situ* mineral precipitation experiment at a deep-sea artificial hydrothermal vent (JAMSTEC 2016). The vent at Hole C0014G discharges fluids from a steel pipe with an 8.89 cm (3.5 inch) inner diameter (Fig. 2). Periodic descaling operations, which are essential to remove hydrothermal precipitates from the pipe and ensure continuous flow, identified by a flame structure and the release of many bubbles (Figs. 2a and 2b), enable research to be done at this vent. During scale-removal operations in early 2016 (Figs. 2c and 2d), a ROV-mounted hydraulic drill was used to retrieve a core sample of hydrothermal sulfide scale from the vent pipe at Hole C0014G. Scale within vent pipes is commonly assumed to form by conductive cooling of hydrothermal fluid under conditions that limit mixing with ambient cold seawater, unlike the more diffuse process typical of a porous chimney on a natural hydrothermal vent. Thus, such scale may accurately record secular changes in the chemical and physical

properties of the hydrothermal fluid. Moreover, hydrothermal scale yields information about the subseafloor conditions and mechanisms of mineral precipitation (e.g., Hardardóttir et al. 2010). In this paper, we report the petrographic, mineralogical, microthermometric, and geochemical features of the hydrothermal scale retrieved from Hole C0014G.

GEOLOGICAL SETTING AND SAMPLING OPERATION

Okinawa Trough

The Okinawa Trough is a back-arc basin within the East China Sea that extends more than 1200 km from the Japanese mainland to Taiwan, west of the Ryukyu Arc (Fig. 1). Active rifting structures associated with magmatism have been reported along the length of the trough (Letouzey and Kimura 1986). A recent multichannel seismic survey in the southern Okinawa Trough recognized an area of crustal thinning from an original thickness of ~25 km to ~12 km beneath the rift axis, as well as a thick layer (~10 km) with a *P*-wave velocity of 6.5–7.2 km/s at the lower crust level, interpreted as mantle material accreted onto the bottom of the crust during crustal stretching (Arai et al. 2017). Given its slow extension rate of 3.7 ± 0.06 cm/yr, documented by Global Navigation Satellite System data (Kotake 2000), the Okinawa Trough is considered to be at the

nascent stage of back-arc basin formation, in transition from continental rifting to seafloor spreading. The detailed tectonic setting, geological features, volcanism, origin, and evolution of the Okinawa Trough are reviewed by Ishibashi et al. (2015) and references therein.

Iheya-North hydrothermal field

The Iheya-North hydrothermal field, the focus area of this study, is located in the middle segment of the Okinawa Trough (Fig. 1a). In the middle to southern Okinawa Trough, the trough axis consists of a set of *en echelon* grabens (Kimura 1985). Although the volcanic front of the Ryukyu Arc is submerged in the middle Okinawa Trough, an area of extensive intra-trough volcanism in the Iheya Graben, known as the volcanic arc migration phenomenon (VAMP), has been interpreted as a consequence of the migration of the volcanic arc into the back-arc basin (Sibuet et al. 1987). Volcanism in the middle Okinawa Trough is characterized as bimodal, with magma compositions ranging from rhyolite to basalt (Ishikawa et al. 1991; Shinjo and Kato 2000; Yamasaki 2017, 2018). The VAMP area is associated with areas of anomalously high heat flow (Masaki et al. 2011; Yamano et al. 1986) and includes several active hydrothermal fields, such as the Izena Hole, Clam field, Iheya-North field, Yoron Hole, and the southern flank of Iheya Minor Ridge

127 (Ishibashi and Urabe 1995; Ishibashi et al. 2015).

128 The Iheya-North hydrothermal field is located on Iheya-North Knoll, about 1000 m
129 below sea level on the eastern slope of a small volcanic knoll (Fig. 1). During cruises
130 CK14-04 and CK16-01 (D/V *Chikyu* Expeditions 907, 9–26 July 2014, and 908, 11
131 February to 17 March 2016, respectively; Yamasaki 2017, 2018), coring confirmed that
132 the Central Valley consists of hemipelagic sediments overlying pumiceous volcaniclastic
133 flow deposits, as previously suggested by the presence of disordered seismic reflectors as
134 deep as 400–500 m below the seafloor (Tsuji et al. 2012). The hydrothermal field of
135 Iheya-North Knoll consists, from north to south, of the Original, Natsu, and Aki Sites
136 (Kasaya et al. 2015; Nakamura et al. 2015); the drilling sites of IODP Expedition 331,
137 including our study area, are all at the Original Site.

138 At the Original Site, more than 10 active hydrothermal mounds associated with
139 sulfide or sulfate mineralization are distributed in a N–S- or NNW–SSE-oriented zone
140 less than 500 m long (Fig. 1). The hottest hydrothermal fluid (311°C) was recorded at the
141 central North Big Chimney (NBC) Mound, which rises ~30 m above the surrounding
142 seafloor (Nakagawa et al. 2005). Rock samples from Iheya-North Knoll obtained during
143 cruises CK14-04 and CK16-01 (D/V *Chikyu* Expeditions 907 and 908) consist of
144 hydrothermally altered rhyolite and a mixture of unaltered and altered pumice (Yamasaki

145 2017, 2018), and have bulk trace element compositions similar to those of Type 2 rhyolite
146 of the middle Okinawa Trough (Shinjo and Kato 2000). Electrical resistivity and spectral
147 induced polarization profiles of drill core samples (Komori et al. 2017), as well as the
148 results of a deep-towed marine electrical resistivity tomography survey, indicate that the
149 Iheya-North hydrothermal field contains multiple layers of low-resistivity sulfide-rich
150 material, both in sulfide mounds on the seafloor and in a discrete sulfide layer about 40
151 m below the seafloor (Ishizu et al. 2019).

152 Samples from mounds and chimneys of Iheya-North Knoll display polymetallic
153 mineralization and are composed mainly of sphalerite, wurtzite, galena, pyrite, marcasite,
154 anhydrite, gypsum, and barite, plus minor chalcopyrite, arsenopyrite, tetrahedrite,
155 luzonite, freieslebenite ($Ag_2Pb_2Sb_2S_6$), rhodochrosite, amorphous silica, realgar, native
156 arsenic, and native sulfur (Ueno et al. 2003). For example, sulfide-rich chimneys formed
157 at artificial hydrothermal vents at Holes C0016A and C0016B are dominated by
158 sphalerite/wurtzite, galena, chalcopyrite, and pyrite/marcasite. In contrast, sulfate-rich
159 chimneys formed at Hole C0013E are dominated by anhydrite, gypsum, and barite with
160 minor unidentified Zn-sulfate minerals, amorphous silica, and talc (Nozaki et al. 2016).
161 During IODP Expedition 331, massive and semi-massive sulfide samples were collected
162 from the western flank of the NBC Mound at Site C0016B (Takai et al. 2011, 2012; Yeats

et al. 2017). These sulfide blocks are characterized by rounded, 1–5 mm fragments of clay-altered and hard siliceous volcanic rock in a matrix of sphalerite (~60%), pyrite (~15%), and quartz, with lesser amounts of galena and chalcopyrite (Yeats et al. 2017). Mineralization ages of barite crystals in natural chimney and mound samples determined by electron spin resonance range from 560 to 4300 yr, a much younger age range than that of samples from the Izena Hole (~16000 yr) (Fujiwara et al. 2015), a site with several hydrothermal mounds and a thick subseafloor sulfide layer. Lead isotopic compositions of galena in drill core samples — recently determined by laser ablation multicollector inductively coupled plasma mass spectrometry — are similar to those of galena in other volcanic rocks in the Okinawa Trough, regardless of their occurrence, paragenesis, or core depth (Totsuka et al. 2019).

In summary, the polymetallic (Cu-Pb-Zn±Au±Ag) mineralization observed in the Iheya-North hydrothermal field is considered to be a modern analogue of Kuroko-type VMS deposits on land (Ishibashi et al. 2015; Nozaki et al. 2016; Yeats et al. 2017).

Sampling

Hydrothermal scale was recovered by ROV hydraulic drill coring from Hole C0014G at the Original Site, at a water depth of 1059.8 m (Figs. 1 and 2c), during D/V *Chikyu*

Expedition 908. The ROV hydraulic short drill, with a stroke length of 12.7 cm (5 inches) and outer diameter of 5.08 cm (2 inches), was used to remove scale from inside the steel vent pipe, although it recovered a plug of scale only 3 cm long and failed to penetrate the blockage (Fig. 3a). The ROV hydraulic long drill (Fig. 2c), with a stroke length of 40.64 cm (16 inches), subsequently succeeded in penetrating the scale deposit, rejuvenating the hydrothermal fluid discharge (Fig. 2d) and recovering a section of scale 20 cm long (Fig. 3b). The recovered samples of hydrothermal scale thus have a total length of 23 cm and a diameter of 4.2 cm, with a narrow central passage. They consisted of seven main blocks, which according to their depth in the pipe were labeled as samples C0014G 0–3 cm, 3–8 cm, 8–11 cm, 11–14 cm, 14–17 cm, 17–20 cm, and 20–23 cm. These samples consisted primarily of massive, dense, gray sphalerite with a semimetallic luster and radially oriented grains (Figs. 3c and 3d). Up to five concentric layers of this material, separated by layers of reddish-brown material less than 1 mm thick, were visible (Figs. 3c and 3d).

In sample C0014G 3–8 cm, which had the narrowest central passage, the mineral precipitation process could be tracked sequentially from rim to core (Fig. 3d). Viewed under a reflected-light polarization microscope, this particular slice of core was dominated by sphalerite, with lesser amounts of galena and chalcopyrite, and minor barite, cotunnite ($PbCl_2$), and unidentified Zn-sulfate and Bi-rich minerals (Fig. 4). The

199 innermost (youngest) scale was rich in dendritic galena with sphalerite and minor
200 cotunnite (layer 1) (Fig. 4a). This layer was enclosed by a porous material rich in
201 botryoidal and anhedral chalcopyrite with minor unidentified Zn-sulfate minerals (layer
202 2), which in turn was enclosed by a sphalerite-rich layer with dendritic galena (layer 3)
203 (Figs. 4a–c). Toward the exterior of the sample (i.e., nearer the wall of the vent pipe), (1)
204 massive, coarse-grained sphalerite-dominant layers (layer 4), alternated with (2) a more
205 porous layer with euhedral galena and chalcopyrite occurring in the pore spaces (layer 5)
206 (Figs. 4a, 4d–f), corresponding to the gray and reddish-brown layers, respectively (Fig.
207 3). The massive sphalerite commonly contained unidentified Bi-rich minerals, typically
208 3–5 μm in size. Radial cracks in the massive sphalerite were filled with euhedral galena
209 and chalcopyrite microcrystals (Fig. 4g). A layer rich in acicular barite crystals (layer B)
210 (Figs. 4h and 4i) visible in the innermost and uppermost parts of the scale sample is
211 attributable to mixing of hydrothermal fluid and ambient cold seawater, which occurred
212 only at the top of the vent pipe (e.g., de Ronde et al. 2003, 2005).
213
214 **ANALYTICAL METHODS**
215 **X-ray diffraction**
216 Samples for X-ray diffraction (XRD) analysis were crushed and pulverized with an agate

217 mortar and pestle. Diffraction data were acquired on a MiniFlex II instrument (Rigaku
218 Corporation Co., Ltd.), installed at the Japan Agency for Marine-Earth Science and
219 Technology (JAMSTEC), using a Cu source, a generator voltage of 30 kV, and a current
220 of 15 mA. The XRD operating conditions were set to step scans from 2 to 90° 2θ in 4400
221 steps at a rate of 2° 2θ/min with a 1.25° divergence slit, 1.25° diffusion slit, and 0.3 mm
222 analytical slit. Diffraction data were analyzed using the manufacturer's diffraction
223 evaluation software (PDXL) in combination with a crystal database from the International
224 Centre for Diffraction Data (https://www.icdd.com/).
225
226 **X-ray fluorescence mapping**
227 Samples of the hydrothermal scale for analysis by X-ray fluorescence (XRF) mapping
228 were cut with a diamond saw and polished with a diamond plate and successive diamond
229 pastes of 70, 30, 13, 6, and 1 μm roughness. Energy-dispersive (ED)-XRF mapping was
230 performed on an EA6000VXF instrument (Hitachi High-Technologies Corporation Co.,
231 Ltd.) at JAMSTEC, a custom-built machine consisting of the EA6000VX unit equipped
232 with a polycapillary X-ray convergence system enabling a minimum X-ray beam size of
233 about 30 μm. X-rays were generated by a Rh source, using a generator voltage of 45 kV
234 and a current of 0.9 mA. The sample stage was moved in 10 μm steps, with each point

235 measured for 20 ms. The scale sample was divided into 81 grid cells of 467 × 467 pixels
236 each to cover the whole surface area, and it took 6520 minutes to obtain the integrated
237 elemental mapping images.
238
239 **Mineral chemistry by electron microprobe**
240 Samples of hydrothermal scale for electron probe microanalysis (EPMA) were cut with a
241 diamond saw, mounted in acrylic resin (Acryl Monomer, Nichika Inc.), similarly polished
242 with a diamond plate and diamond pastes of 70, 30, 13, 6 and 1 μm roughness, and carbon-
243 coated. Chemical compositions of constituent minerals (Supplementary Table 1) were
244 determined on the JEOL JXA-8530F EPMA equipped with a field-emission source at
245 Kyushu University operating with an accelerating voltage of 20 kV and a beam current
246 of 10 nA. The incident electron beam was focused to a diameter of 100 nm, and the
247 counting time was 40 s for each element. The acquired X-ray intensities were corrected
248 by the ZAF method (Castaing 1951).
249
250 **Fluid inclusion microthermometry**
251 Fluid inclusions in sphalerite were heated to homogenization to estimate the formation
252 temperature of the host mineral. Polished sections 150–250 μm thick were prepared for

analysis using a diamond plate and diamond pastes of 70, 30, 13, 6, and 1 μm roughness on both faces of the wafers. Microthermometric measurements of fluid inclusions (homogenization temperature T_h, and last ice melting temperature Tm_{ice}; Supplementary Table 2) were made using a Linkam 10036L heating/freezing system mounted on a Zeiss optical microscope equipped with 50x objective lenses at JAMSTEC. The stage was calibrated to the melting point of pure water ice. Heating rates were 1–5 and 0.1–0.2 °C/min for T_h and Tm_{ice} determinations, respectively; errors on T_h and Tm_{ice} were typically ±0.1°C (Saito et al. 2016). The salinity of water in the inclusions was calculated from the depression of the freezing point (Bodnar 1993).

Bulk geochemistry by inductively coupled plasma mass spectrometry

Major and trace element analyses were performed by inductively coupled plasma-mass spectrometry (ICP-MS) on an Agilent 7500ce instrument installed at JAMSTEC. Seven subsamples of hydrothermal scale were cut with a diamond saw and pulverized with an agate mortar and pestle. Powdered samples weighing ~50 mg were dissolved using the HNO_3-$HClO_4$-HF digestion method in Teflon PFA screw-cap beakers, then heated overnight on a hot plate at 110°C. The digested samples were progressively evaporated at 110°C for more than 12 h, 130°C for 3 h, and 160°C until dryness. The residue was

dissolved in 5 mL Milli-Q deionized water combined with 4 mL HNO_3 and 1 mL HCl, then further diluted to 1:100 by mass (total dilution factor ~20000) before introduction into the ICP-MS instrument. Details of these analytical procedures, including instrumental drift and mass interference correction methods, are reported in Takaya et al. (2018).

Crystallography

The crystallography of scale samples was analyzed by scanning electron microscope (SEM) observations and electron backscatter diffraction (EBSD) analyses using the field-emission SEM (JEOL JSM-7001F) at Tohoku University. The scale samples were cut with a diamond saw and polished with diamond pastes of 3 and 1 μm, then further polished with a 0.04 μm colloidal silica suspension to remove any damaged layers. The samples were then coated with a platinum film to minimize electron charging. EBSD data were obtained with a Nordlys camera (Oxford Instruments Co., Ltd.) under an accelerating voltage of 15 kV and a beam current of 6.0 nA, with step intervals of 15 μm and a total working distance of 25 mm. Data collection and EBSD analyses were performed with the Channel 5 analysis suite from HKL Technology (Oxford Instruments) and sphalerite crystal structure data from Skinner (1961).

RESULTS AND DISCUSSION

Petrographic features and sphalerite compositions

On X-ray diffractograms of the hydrothermal scale (Supplementary Fig. 1), sphalerite peaks predominate, with lesser peaks for galena and chalcopyrite. Whereas the ideal diffraction pattern of sphalerite has the strongest peak at 28.6° (the d_{111} reflection), the strongest peak in this sample was at 47.5° (the d_{022} reflection) with an intensity 1.4 to 3.3 times that of the 28.6° peak. We attribute this anomaly to cleavage that developed parallel to the {100} plane during the preparation of the powdered sample.

The ED-XRF maps of Pb, Zn, and Fe clearly display alternating layers of gray and reddish-brown components in the scale (Fig. 5). At least seven layers relatively rich in Pb were apparent across the thickness of the sample. The innermost two (i.e., labeled 1 and 2 in Fig. 5) correspond to layers 1 and 3, respectively, in the microscope images (Figs. 4a and 4c), i.e., the innermost layer rich in dendritic galena with sphalerite and minor cotunnite, and the sphalerite-rich layer with dendritic galena, respectively. The other five of these seven layers (i.e., 3–7 in Fig. 5) correspond to the porous reddish-brown component, which is rich in galena and chalcopyrite (layer 5 in Figs. 4e and 4f). The Zn and Fe maps display several Zn-poor and Fe-rich radial cracks that correspond to the

307 cracks filled with galena and chalcopyrite observed under the microscope (see Fig. 4g);
308 this texture is similar to the quench texture of a molten sulfur sample obtained from Sulfur
309 Cauldron, Daikoku volcano (de Ronde et al. 2015).

310 Sphalerite in the scale showed a broad range of Fe and Mn contents (Supplementary
311 Table 1). Grains of pure sphalerite (>96 wt% total values in EPMA analyses) in the
312 innermost layer rich in dendritic galena (layer 1 in Figs. 4a and 6a) had Fe contents of
313 5.09–11.0 wt% (average 7.39 ± 1.44 wt%, 1SD; n = 36) and Mn contents of 0.58–1.16
314 wt% (0.88 ± 0.13 wt%). In contrast, sphalerite in the gray component (layer 4 in Figs. 4d
315 and 6b) had, on average, lower Fe contents of 2.02–5.06 wt% (2.97 ± 0.69 wt%; n = 138)
316 and Mn contents of 0.26–0.75 wt% (0.42 ± 0.09 wt%). Sphalerite in the reddish-brown
317 component (layer 5 in Figs. 4e, 4f, and 6c) had similarly low Fe contents of 1.77–6.69
318 wt% (4.23 ± 1.20 wt%; n = 94) but high Mn contents of 0.26–0.89 wt% (0.58 ± 0.16 wt%).
319 These Fe and Mn contents are strongly correlated (r^2 = 0.93), with some overlap among
320 the three sphalerite groups (Fig. 6d).

321 The mole fraction of Fe in sphalerite is often used to estimate the sulfur fugacity of
322 hydrothermal fluids when the fluid temperature is well constrained (Barton and Toulmin
323 1966). The temperature of the hydrothermal fluid discharging from Hole C0014G was
324 measured at 304–311°C by IODP Expedition 331 (Kawagucci et al. 2013); this

325 temperature is consistent with the results of our analysis of sphalerite fluid inclusions (see
326 next subsection). The calculated sulfur fugacity of the hydrothermal fluid forming the
327 sphalerite in the gray component (Fig. 6b) is very similar to that determined from chimney
328 samples from natural deep-sea hydrothermal vents (e.g., Suzuki et al. 2008), whereas the
329 calculated sulfur fugacity of the sphalerite in the reddish-brown component (Fig. 6c) is
330 substantially lower (Fig. 6e). Given the nearly constant post-drilling temperature of the
331 discharge from Hole C0014G (Kawagucci et al. 2013), it appears that changes in sulfur
332 fugacity alone might account for the formation of the concentric layers found in the scale.
333 In the innermost (youngest) part of the scale sample, a rare lead-chloride mineral
334 commonly appeared in the SEM images (Figs. 7a and 7b), confirmed by the energy
335 dispersive X-ray spectroscopy (EDS) equipped with SEM results in which only peaks of
336 Pb and Cl were detected. The mineral has an acicular habit and is closely associated with
337 sphalerite (Fig. 7b). We identify it as cotunnite ($PbCl_2$), a mineral known to form in the
338 periphery of subaerial fumaroles when chloride ion activity is high (e.g., Bridges et al.
339 2012). Typically, anglesite ($PbSO_4$), a secondary mineral after galena, is much more
340 common than cotunnite in modern seafloor hydrothermal deposits (e.g., Fallon et al.
341 2017; Nozaki et al. 2016) owing to the abundant sulfate ion availability in seawater. The
342 steel pipe at Hole C0014G appears to largely isolate the hydrothermal fluid from the

343 ambient seawater, leading to lower [SO_4^{2-}] activity and relatively higher [Cl^-] activity in
344 the discharging fluid compared with their activities in a natural hydrothermal vent. At the
345 pH of the hydrothermal fluid emanating from this hole (4.7–5.0; Kawagucci et al. 2013),
346 Pb compounds can exist either as anglesite or Pb-chloride complexes (Supplementary
347 Figs. 2a and 2b). Thus, cotunnite is favored within the drill pipe, where mixing with the
348 ambient cold seawater is limited, unlike conditions in natural hydrothermal vents and
349 chimneys.
350
351 **Microthermometry of fluid inclusions**
352 The shallowest (uppermost) and deepest scale segments (samples C0014G 0–3 cm and
353 C0014G 20–23 cm) were selected for fluid inclusion analysis. Although these segments
354 had larger central orifices than sample C0014G 3–8 cm (Fig. 3), they each contained at
355 least three alternating layers of gray and reddish-brown material (Figs. 8a and 8b). We
356 were unable to analyze the sphalerite in the reddish-brown component because of its
357 higher Fe content and insufficient transparency. In Fe-poor, transparent sphalerite crystals,
358 numerous fluid inclusions were observed as well-isolated primary inclusions; at room
359 temperature, they comprised mainly liquid-rich, two-phase inclusions, as well as
360 decrepitated inclusions and minor amounts of inclusions with necking-down features. The

361 sizes of the analyzed inclusions ranged from 5–50 μm, and they had triangular, square, or
362 elongate to irregular shapes. The $V/(V + L)$ ratios (where V and L are the volumes of the
363 vapor and liquid, respectively) determined under the microscope ranged from 0.2 to 0.5,
364 typically 0.25 or 0.3, and all two-phase inclusions homogenized into the liquid phase after
365 heating. The homogenization temperature (T_h) of the inclusions ranged from 279 to 330°C
366 (314 ± 8°C, 1 SD; n = 35) (Fig. 8c, Supplementary Table 2). The average homogenization
367 temperature of 314°C is only slightly higher than the measured temperature of the
368 hydrothermal fluid (304–311°C) at Hole C0014G (Kawagucci et al. 2013). The ice
369 melting temperature ($T\mathrm{m}_{\mathrm{ice}}$) ranged from –2.9 to –1.8°C (–2.3 ± 0.3°C; n = 38),
370 corresponding to a salinity of 3.1–4.8 NaCl equivalent wt% (3.8 ± 0.5 NaCl eq. wt%; n =
371 38) (Fig. 8d), or ~0.96–1.5 times that of seawater (~3.2 wt%). The average salinity in the
372 inclusions was thus about 96% to 150% that of seawater, with the lower end of the range
373 consistent with the Cl concentration of the hydrothermal fluids discharging from Hole
374 C0014G, which ranged from 574 to 596 mM, or 106–110% of the seawater value of 540
375 mM. However, the upper salinity range of the fluid inclusions was noticeably higher than
376 seawater salinity, indicating that the two-phase separation resulted from boiling of the
377 hydrothermal fluid beneath the seafloor (e.g., de Ronde et al. 2003). This result is
378 consistent with the observed release of many bubbles and the flame structure of the

379 hydrothermal fluid discharging from the artificial hydrothermal vent (Figs. 2a and 2b).

380

381 **Bulk geochemistry**

382 The bulk compositions determined by ICP-MS showed that the scale was very rich in Zn
383 (56.5–59.0 wt%; n = 7) with lesser amounts of Fe (2.68–3.21 wt%), Pb (0.75–2.36 wt%),
384 Mn (0.35–0.37 wt%), Cd (0.30–0.32 wt%), Cu (0.07–0.54 wt%), Ag (18.0–41.0 ppm),
385 and Au (<0.4 ppm) (Figs. 9 and 10, Supplementary Table 3). This chemical profile is
386 consistent with the petrographic observations (Fig. 4) and the low Fe content of the
387 sphalerite in the gray component (Fig. 6d). The EPMA results indicate that most of the
388 Mn and Cd in the scale was contained within sphalerite (Supplementary Table 1). The Ba
389 content exceeded 300 ppm only in the uppermost sample (sample C0014G 0–3 cm) (Fig.
390 10), and Sr was also detected only in this sample; these results are consistent with barite
391 formation due to limited mixing between hydrothermal fluid and ambient seawater only
392 at the top surface of the vent pipe (Figs. 4h and 4i). Consistent with the absence of
393 anhydrite and gypsum in the petrographic studies, calcium was not detected in any of the
394 samples. Zinc and Cd contents exceeded the average composition of the upper continental
395 crust by five orders of magnitude (Fig. 9), not surprising given the overwhelming
396 predominance of sphalerite in the samples. The lead content of the scale exceeded that of

397 seafloor hydrothermal deposits on the East Pacific Rise (EPR) and Besshi-type VMS
398 deposits, whereas the contents of all other elements were lower than those in EPR
399 hydrothermal deposits, Kuroko- and Besshi-type VMS deposits on land, and sulfide-rich
400 parts of chimneys formed on deep-sea artificial hydrothermal vents (Fig. 9). Although the
401 examined hydrothermal scale deposit was only 23 cm long, several elements clearly show
402 changes with depth below the pipe top (Fig. 10). Although Zn and Pb displayed no clear
403 trends with depth, Fe and Cu contents increased with depth, Sb decreased with depth, and
404 Ba was present only in the topmost sample. These findings suggest that chalcopyrite
405 ($CuFeS_2$) increased in abundance with depth down the drill pipe (artificial vent) at Hole
406 C0014G, and that a thermal gradient over a depth interval of only 23 cm partly controlled
407 the abundances of the various minerals. They also suggest that scale with an even higher
408 Cu content may have precipitated in the pipe deeper beneath the seafloor. For comparison,
409 at Hole C0016A, unfiltered hydrothermal fluid from the artificial deep-sea hydrothermal
410 vent, including suspended particles, contains 0.54 ppm Cu, 1.61 ppm Pb, and 5.07 ppm
411 Zn (Nozaki et al. 2016).

412 These results from two different artificial vents confirm that Zn concentrations exceed
413 Cu concentrations by an order of magnitude at the Original Site of Iheya-North Knoll.
414 Considering the respective solubilities of Zn and Cu (see Fig. 24 of Hannington et al.

415 1995), the measured temperature range (304–311°C) and pH (4.7–5.0) of the
416 hydrothermal fluid at Hole C0014G (Kawagucci et al. 2013), and the boiling point of
417 ~317°C at the water depth of Hole C0014G, the material precipitated within the vent pipe
418 is expected to be Zn-rich with less Cu. Moreover, scale richer in Cu might be precipitating
419 deeper within the pipe.
420
421 **Formation mechanism of concentric layers**
422 The scale sample contained as many as seven concentric layers (Figs. 3 and 5). A polished
423 thin section of sample C0014G 8–11 cm showed at least five concentric layers, with the
424 reddish-brown component increasing in abundance toward the margin of each concentric
425 layer (Supplementary Fig. 3). The sphalerite crystals exhibited weak optical anisotropy
426 as a result of the development of {111} twin lamellae. Although the crystals displayed
427 irregular cross sections, they were elongated in the radial direction. SEM images of
428 sphalerite crystals from the inner edge of the same scale sample showed both tabular and
429 columnar crystal shapes with major {111} faces (Figs. 11a and 11b) on which growth
430 steps of varied thickness were observed. EBSD results also showed that these tabular
431 sphalerite crystals had well-developed {111} faces and grew toward the ⟨110⟩ direction
432 (Supplementary Fig. 3). The grain size of sphalerite also changed across the concentric

433 layers. For example, near the boundary between the gray and reddish-brown components,
434 the grain size of sphalerite decreased from 100–300 μm to several tens of micrometers
435 (Analytical area 3 in Supplementary Fig. 3), and even smaller crystals occupied the void
436 spaces along this boundary (Fig. 11). The smallest sphalerite crystals had tabular forms
437 or striated surfaces due to {111} twinning (Figs. 11c and 11d). The crystallographic
438 orientations of sphalerite crystals were aligned with their growth directions. This
439 alignment grew stronger toward the inner side of the sample (Supplementary Fig. 3).
440 The formation of concentric layers in the scale appears to be related to scale removal
441 operations. Between the installation of the guidebase and casing pipe at Hole C0014G in
442 September 2010, during IODP Expedition 331, and the collection of our sample during
443 cruise CK16-01 (D/V *Chikyu* Expedition 908) in February 2016, seven semi-annual
444 research cruises (i.e., NT11-16, NT12-06, NT12-23, NT13-23, KY14-01, NT15-02, and
445 NT16-02) visited the hole with a ROV. During these seven cruises, researchers used a
446 hydraulic hammer and chisel to remove parts of the scale (Figs. 2a and 2b) to obtain
447 samples of chimney material formed on the vent pipe and pristine hydrothermal fluid, and
448 they also performed various *in-situ* geochemical, geophysical, and ecological
449 experiments (e.g., Kawagucci et al. 2013; Nakajima et al. 2015; Nozaki et al. 2016;
450 Takahashi et al. 2020; Thornton et al. 2015; Yamamoto et al. 2013). These regular

451 operations changed conditions within the pipe from (1) an almost fully clogged
452 hydrothermal pathway with weak hydrothermal shimmering to (2) an open pipe with
453 vigorous hydrothermal discharge (Fig. 12). Within the clogged pipe, mixing between
454 seawater and hydrothermal fluid could occur only at the top surface of the vent pipe and
455 the sulfur fugacity of the hydrothermal fluid was low (Fig. 12a). Under these conditions,
456 sphalerite crystals with relatively high Fe content precipitated (Figs. 6d and 6e), and the
457 relatively high [Cl^-] and low [SO_4^{2-}] activities led to the precipitation of cotunnite (Fig.
458 7 and Supplementary Fig. 2). The observation that Fe content is highest in the innermost
459 scale (Fig. 6d) is consistent with a clogged vent pipe inhibiting mixing between
460 hydrothermal fluid and ambient seawater and inducing low sulfur fugacity in the
461 hydrothermal fluid. Boiling and phase separation occurring beneath the recovered scale
462 sample resulted in the formation of hydrothermal brine, as confirmed by the fluid
463 inclusion analysis (Fig. 8d, Supplementary Table 2), with lower sulfur fugacity and higher
464 [Cl^-] activity, because the vapor phase could pass through cracks and porous parts of the
465 scale more easily than the liquid phase. Indeed, as the ROV approached the pipe at Hole
466 C0014G to perform descaling, many bubbles were observed to be rising from the pipe
467 into the seawater (Fig. 2a). Petrographic and geochemical evidence from the scale
468 suggests that the reddish-brown components were deposited during times when the pipe

469 was clogged.

470 After the descaling, the hydrothermal fluid discharge became vigorous (Figs. 2b and
471 2d). This vigorous hydrothermal discharge may have induced local seawater recharge
472 (e.g., Caratori Tontini et al. 2019) through the subseafloor base of the casing pipe to
473 maintain conservation of mass (Fig. 12b), which in turn raised the sulfur fugacity in the
474 hydrothermal fluid and led to the precipitation of sphalerite with lower Fe contents (Figs.
475 6d and 6e). It was during this phase that the dark gray component was deposited in the
476 pipe. These artificial changes in the pipe interior explain how changes in sulfur fugacity
477 led to different scale compositions and mineral assemblages even as the temperature
478 remained relatively constant at the ambient boiling point (Fig. 12). Thus, it would appear
479 that the scale has indeed recorded a history of hydrological changes induced by periodic
480 descaling.

481

482 **CONCLUSIONS**

483 Hydrothermal scale recovered from the vent pipe of the artificial deep-sea hydrothermal
484 vent at Hole C0014G contained at least five concentric layers, alternating between (1)
485 porous, reddish-brown, relatively Fe-rich sphalerite rich in galena and chalcopyrite and
486 (2) massive, gray, relatively Fe-poor sphalerite. Cotunnite ($PbCl_2$) was identified in the

487 innermost part of the scale, associated with Fe-rich sphalerite. Sphalerite fluid inclusions
488 had average homogenization temperatures of 314 ± 8°C and salinities of 3.8 ± 0.5 wt%
489 NaCl equivalent, consistent with the temperature of the hydrothermal fluid discharging
490 from Hole C0014G. Salinity in the fluid inclusions was noticeably higher than that of
491 seawater, indicating that boiling and phase separation occurs beneath the seafloor. The
492 bulk scale was dominated by Zn (56.5–59.0 wt%) with lesser amounts of Fe (2.68–3.21
493 wt%), Pb (0.75–2.36 wt%), Mn (0.35–0.37 wt%), Cd (0.30–0.32 wt%), Cu (0.07–0.54
494 wt%), Ag (18.0–41.0 ppm), and Au (<0.4 ppm). Fe and Cu contents, corresponding to
495 chalcopyrite, increased with depth in the examined scale sample; thus, we infer that scale
496 precipitating deeper in the vent pipe (or in the subseafloor casing) may have higher Cu
497 contents because of the higher fluid temperature in deeper parts. The concentric layers in
498 the hydrothermal scale appear to have formed as a consequence of scale removal
499 operations during seven previous research cruises. Alternation between relatively clogged
500 (closed) and open pipe conditions induced boiling and phase separation in the
501 hydrothermal fluid and affected the fluid composition, thus inducing the precipitation of
502 different mineral assemblages. Changes of the Fe contents of the sphalerite scale are
503 inferred to be due to the introduction of ambient seawater through local recharge as a
504 consequence of reinvigorated fluid flow. The hydrothermal scale thus records the history

505 of hydrological changes induced by scale removal operations.

506

507 **Acknowledgments** We thank Yukari Otsuki and Hideo Yamamoto of JAMSTEC for
508 supporting ICP-MS analyses at JAMSTEC. We also thank the officers, crew, scientists,
509 and ROV operating teams of cruises NT16-02 and CK16-01 (D/V *Chikyu* Expedition
510 908) for their valuable collaborations. We are grateful to Terence Lim and other engineers
511 at NuStar Technologies Pte. for their helpful engineering support in the development of
512 the ROV hydraulic tools. Careful review and constructive comments by Dr. Cornel de
513 Ronde much improved the original manuscript. Instrumentation for the fluid inclusion
514 analysis at JAMSTEC was supported by KAKENHI grant JP25707038 to Takazo Shibuya
515 of JAMSTEC.

516

517 **Electronic supplementary material** The online version of this article
518 (https://doi.org/10.1007/xxxx) contains supplementary material, which is available to
519 authorized users.

520

REFERENCES

Arai R, Kodaira S, Kaiho Y, Takahashi T, Miura S, Kaneda Y (2017) Crustal structure of the southern Okinawa Trough: Symmetrical rifting, submarine volcano, and potential mantle accretion in the continental back-arc basin. J Geophys Res 122(1):622–641. https://doi.org/10.1002/2016JB013448

Barton PB, Toulmin P (1966) Phase relations involving sphalerite in the Zn-Fe-S system. Econ Geol 61(5):815–849. https://doi.org/10.2113/gsecongeo.61.5.815

Beaulieu SE, Baker ET, German CR (2015) Where are the undiscovered hydrothermal vents on oceanic spreading ridges? Deep Sea Res II 121:202–212. https://doi.org/10.1016/j.dsr2.2015.05.001

Bodnar RJ (1993) Revised equation and table for determining the freezing point depression of H_2O-NaCl solutions. Geochim Cosmochim Acta 57(3):683–684. https://doi.org/10.1016/0016-7037(93)90378-A

Bridges TF, Turner R, Rumsey MS (2012) A geochemical study of the lead oxychloride mineral assemblage of the Mendip Hills, Somerset, UK using a stability field model. J Russell Soc 15:18–28.

Caratori Tontini F, Tivey MA, de Ronde CEJ, Humphris SE (2019) Heat flow and near‐seafloor magnetic anomalies highlight hydrothermal circulation at Brothers volcano caldera, southern Kermadec arc, New Zealand. Geophys Res Lett 46(14): 8252–8260. https://doi.org/10.1029/2019GL083517

Castaing R (1951) Application of electron probes to local chemical and crystallographic analysis. Dissertation, University of Paris.

de Ronde CEJ, Chadwick WW, Ditchburn RG, Embley RW, Tunnicliffe V, Baker ET, Walker SL, Ferrini VL, Merle SM (2015) Molten sulfur lakes of intraoceanic arc volcanoes. In: Rouwet D, Christenson B, Tassi F, Vandelbroulemuck J (eds) Volcanic lakes. Springer-Verlag, Berlin, Heidelberg, pp 261–288. https://doi.org/10.1007/978-3-642-36833-2_11

de Ronde CEJ, Faure K, Bray CJ, Chappell DA, Wright IC (2003) Hydrothermal fluids associated with seafloor mineralization at two southern Kermadec arc volcanoes, offshore New Zealand. Mineral Deposita 38(2): 217–233. https://doi.org/10.1007/s00126-002-0305-4

de Ronde CEJ, Hannington MD, Stoffers P, Wright IC, Ditchburn RG, Reyes AG, Baker ET, Massoth GJ, Lupton JE, Walker SL, Greene RR, Soong CWR, Ishibashi J, Lebon

GT, Bray CJ, Resing JA (2005) Evolution of a submarine magmatic-hydrothermal system: Brothers volcano, southern Kermadec arc, New Zealand. Econ Geol 100(6): 1097–1133. https://doi.org/10.2113/gsecongeo.100.6.1097

Fallon EK, Petersen S, Brooker RA, Scott TB (2017) Oxidative dissolution of hydrothermal mixed-sulphide ore: An assessment of current knowledge in relation to seafloor massive sulphide mining. Ore Geol Rev 86:309–337. https://doi.org/10.1016/j.oregeorev.2017.02.028

Fouquet Y, Charlou JL, Stackelberg U von, Wiedicke M, Erzinger J, Herzig PM, Muehe R (1993) Metallogenesis in back-arc environments: The Lau basin example. Econ Geol 88(8):2154–2181. https://doi.org/10.2113/gsecongeo.88.8.2154

Franklin JM, Gibson HL, Jonasson IR, Galley AG (2005) Volcanogenic massive sulfide deposits. Econ Geol 100th Anniversary Volume:523–560.

Fujiwara T, Toyoda S, Uchida A, Ishibashi J-i, Nakai S, Takamasa A (2015) ESR dating of barite in sea-floor hydrothermal sulfide deposits in the Okinawa Trough. In: Ishibashi J-i, Okino K, Sunamura M (eds) Subseafloor biosphere linked to hydrothermal systems. Springer, New York, pp 369–386. https://doi.org/10.1007/978-4-431-54865-2_29

Hannington M, Jamieson J, Monecke T, Petersen S, Beaulieu S (2011) The abundance of seafloor massive sulfide deposits. Geology 39(12):1155–1158. https://doi.org/10.1130/G32468.1

Hannington MD, Jonasson IR, Herzig PM, Petersen S (1995) Physical and chemical processes of seafloor mineralization at mid-ocean ridges. AGU Geophys Monogr 91:115–157. https://doi.org/10.1029/GM091p0115

Hardardóttir V, Hannington M, Hedenquist J, Kjarsgaard I, Hoal K (2010) Cu-rich scales in the Reykjanes geothermal system, Iceland. Econ Geol 105(6):1143–1155. https://doi.org/10.2113/econgeo.105.6.1143

Ishibashi J-i, Ikegami F, Tsuji T, Urabe T (2015) Hydrothermal activity in the Okinawa Trough back-arc basin: Geological background and hydrothermal mineralization. In: Ishibashi J-i, Okino K, Sunamura M (eds) Subseafloor biosphere linked to hydrothermal systems. Springer, New York, pp 337–359. https://doi.org/10.1007/978-4-431-54865-2_27

Ishibashi J, Urabe T (1995) Hydrothermal activity related to arc-backarc magmatism in the Western Pacific. In: Taylor B (ed) Backarc basins: Tectonics and magmatism, Plenum Press, New York, pp. 451–495. https://doi.org/10.1007/978-1-4615-1843-3_13

Ishikawa M, Sato H, Furukawa M, Kimura M, Kato Y, Tsugaru R, Shimamura K (1991)

593 Report on DELP 1988 cruises in the Okinawa Trough Part 6: petrology of volcanic
594 rocks. Bull ERI Univ Tokyo 66:151–177.
595 Ishizu K, Goto T, Ohta Y, Kasaya T, Iwamoto H, Vachiratienchai C, Siripunvaraporn W,
596 Tsuji T, Kumagai H, Koike K (2019) Internal structure of a seafloor massive sulfide
597 deposit by electrical resistivity tomography, Okinawa Trough. Geophys Res Lett
598 46(20):11025–11034. https://doi.org/10.1029/2019GL083749
599 Japan Agency for Marine-Earth Science and Technology (2016) Sulfide-rich chimney on
600 artificial seafloor rapidly growing -Kuroko-ore cultivation project to start on a full-
601 scale-. JAMSTEC press release on Feb. 25 2016,
602 http://www.jamstec.go.jp/e/about/press_release/20160225_2/
603 Kasaya T, Machiyama H, Kitada K, Nakamura K (2015) Trial exploration for
604 hydrothermal activity using acoustic measurements at the North Iheya Knoll.
605 Geochem J 49(6):597–602. https://doi.org/10.2343/geochemj.2.0389
606 Kawagucci S, Miyazaki J, Nakajima R, Nozaki T, Takaya Y, Kato Y, Shibuya T, Konno
607 U, Nakaguchi Y, Hatada K, Hirayama H, Fujikura K, Furushima Y, Yamamoto H,
608 Watsuji T, Ishibashi J, Takai K (2013) Post-drilling changes in fluid discharge,
609 mineral deposition patterns and fluid chemistry for the seafloor hydrothermal activity
610 in the Iheya-North hydrothermal field, Okinawa Trough. Geochem Geophys Geosyst
611 14(11):4774–4990. https://doi.org/10.1002/2013GC004895
612 Kimura M (1985) Back-arc rifting in the Okinawa Trough. Mar Petrol Geol 2(3):222–
613 240. https://doi.org/10.1016/0264-8172(85)90012-1
614 Komori S, Masaki Y, Tanikawa W, Torimoto J, Ohta Y, Makio M, Maeda L, Ishibashi J-i,
615 Nozaki T, Tadai O, Kumagai H (2017) Depth profiles of resistivity and spectral IP
616 for active modern submarine hydrothermal deposits: a case study from the Iheya
617 North Knoll and the Iheya Minor Ridge in Okinawa Trough, Japan. Earth Planets
618 Space 69:114. https://doi.org/10.1186/s40623-017-0691-6
619 Kotake Y (2000) Study on the tectonics of western Pacific region derived from GPS data
620 analysis. Bull ERI Univ Tokyo 75:229–334.
621 Letouzey J, Kimura M (1986) The Okinawa Trough: genesis of a backarc basin
622 developing along a continental margin. Tectonophysics 125(1-3):209–230.
623 https://doi.org/10.1016/0040-1951(86)90015-6
624 Masaki Y, Kinoshita M, Inagaki F, Nakagawa S, Takai K (2011) Possible kilometer-scale
625 hydrothermal circulation within the Iheya-North field, mid-Okinawa Trough, as
626 inferred from heat flow data. JAMSTEC Rep Res Dev 12:1–12.
627 https://doi.org/10.5918/jamstecr.12.1
628 Mosier DL, Berger VI, Singer DA (2009) Volcanogenic massive sulfide deposits of the

629 world: Database and grade and tonnage models. USGS Open-File Report: 2009-1034.
630 Nakagawa S, Takai K, Inagaki F, Chiba H, Ishibashi J-I, Kataoka S, Hirayama H, Nunoura
631 T, Horikoshi K, Sako Y (2005) Variability in microbial community and venting
632 chemistry in a sediment-hosted backarc hydrothermal system: impacts of subseafloor
633 phase separation. FEMS Microbiol Ecol 54(1):141–155.
634 https://doi.org/10.1016/j.femsec.2005.03.007
635 Nakajima R, Yamamoto H, Kawagucci S, Takaya Y, Nozaki T, Chen C, Fujikura K, Miwa
636 T, Takai K (2015) Post-drilling changes in seabed landscape and megabenthos in a
637 deep-sea hydrothermal system, the Iheya North field, Okinawa Trough. PLoS ONE
638 10(4): e0123095. https://doi.org/10.1371/journal.pone.0123095
639 Nakamura K, Kawagucci S, Kitada K, Kumagai H, Takai K, Okino K (2015) Water
640 column imaging with multibeam echo-sounding in the mid-Okinawa Trough:
641 Implications for distribution of deep-sea hydrothermal vent sites and the cause of
642 acoustic water column anomaly. Geochem J 49(6):579–596.
643 https://doi.org/10.2343/geochemj.2.0387
644 Nozaki T (2008) Geochronology and genesis of the Besshi-type massive sulfide deposits
645 based on the Re-Os isotope system. Dissertation, The University of Tokyo.
646 Nozaki T, Kato Y, Suzuki K (2013) Late Jurassic ocean anoxic event: evidence from
647 voluminous sulphide deposition and preservation in the Panthalassa. Sci Rep 3: 1889.
648 https://doi.org/10.1038/srep01889
649 Nozaki T, Ishibashi J-I, Shimada K, Nagase T, Takaya Y, Kato Y, Kawagucci S, Watsuji
650 T, Shibuya T, Yamada R, Saruhashi T, Kyo M, Takai K (2016) Rapid growth of
651 mineral deposits at artificial seafloor hydrothermal vents. Sci Rep 6:22163. doi:
652 10.1038/srep22163. https://doi.org/10.1038/srep22163
653 Nozaki T, Nagase T, Ushikubo T, Shimizu K, Ishibashi J-I, the D/V Chikyu Expedition
654 909 Scientists (*in press*) Microbial sulfate reduction plays an important role at the
655 initial stage of subseafloor sulfide mineralization. Geology xx(xx): xxx–xxx.
656 https://doi.org/10.1130/G47943.1
657 Piercey SJ (2011) The setting, style, and role of magmatism in the formation of
658 volcanogenic massive sulfide deposits. Mineral Deposita 46(5-6):449–471.
659 https://doi.org/10.1007/s00126-011-0341-z
660 Saito T, Shibuya T, Komiya T, Kitajima K, Yamamoto S, Nishizawa M, Ueno Y,
661 Kurosawa M, Maruyama S (2016) PIXE and microthermometric analyses of fluid
662 inclusions in hydrothermal quartz from the 2.2 Ga Ongeluk Formation, South Africa:
663 Implications for ancient seawater salinity. Precambrian Res 286:337–351.
664 https://doi.org/10.1016/j.precamres.2016.10.003

665 Shinjo R, Kato Y (2000) Geochemical constraints on the origin of bimodal magmatism at
666 the Okinawa Trough, an incipient back-arc basin. Lithos 54(3-4):117–137.
667 https://doi.org/10.1016/S0024-4937(00)00034-7
668 Sibuet J-C, Letouzey J, Barbier F, Charvet J, Foucher J-P, Hilde T, Kimura M, Ling-Yun
669 C, Marsset B, Muller C, Stephan J-F (1987) Back arc extension in the Okinawa
670 Trough. J Geophys Res 92(B13):14041–14063.
671 https://doi.org/10.1029/JB092iB13p14041
672 Skinner BJ (1961) Unit-cell edges of natural and synthetic sphalerites. Am Mineral 46(11-
673 12):1399–1411.
674 Suzuki R, Ishibashi J-I, Nakaseama M, Konno U, Tsunogai U, Gena K, Chiba H (2008)
675 Diverse range of mineralization induced by phase separation of hydrothermal fluid:
676 Case study of the Yonaguni Knoll IV hydrothermal field in the Okinawa Trough
677 back-arc basin. Resour Geol 58(3):267–288. https://doi.org/10.1111/j.1751-
678 3928.2008.00061.x
679 Takahashi T, Yoshino S, Takaya Y, Nozaki T, Ohki K, Ohki T, Sakka T, Thornton B (2020)
680 Quantitative in situ mapping of elements in deep-sea hydrothermal vents using laser-
681 induced breakdown spectroscopy and multivariate analysis. Deep Sea Res I
682 158:103232. https://doi.org/10.1016/j.dsr.2020.103232
683 Takai K, Mottl MJ, Nielsen SH, the Expedition 331 Scientists (2011) Proc IODP 331.
684 Tokyo (Integrated Ocean Drilling Program Management International, Inc.).
685 https://doi:10.2204/iodp.proc.331.2011
686 Takai K., Mottl MJ, Nielsen SHH, the IODP Expedition 331 Scientists (2012) IODP
687 Expedition 331: Strong and expansive subseafloor hydrothermal activities in the
688 Okinawa Trough. Sci Drill 13:19–27. https://doi.org/10.2204/iodp.sd.13.03.2011
689 Takaya Y, Yasukawa K, Kawasaki T, Fujinaga K, Ohta J, Usui Y, Nakamura K, Kimura
690 J-I, Chang Q, Hamada M, Dodbiba G, Nozaki T, Iijima K, Morisawa T, Kuwahara T,
691 Ishida Y, Ichimura T, Kitazume M, Fujita T, Kato Y (2018) The tremendous potential
692 of deep-sea mud as a source of rare-earth elements. Sci Rep 8:5763.
693 https://doi.org/10.1038/s41598-018-23948-5
694 Taylor SR, McLennan SM (1985) The continental crust: Its composition and evolution.
695 Blackwell, Malden, Mass.
696 Thornton B, Takahashi T, Sato T, Sakka T, Tamura A, Matsumoto A, Nozaki T, Ohki T,
697 Ohki K (2015) Development of a deep-sea Laser-induced breakdown spectrometer
698 for in situ multi-element chemical analysis. Deep Sea Res I 95:20–36.
699 https://doi.org/10.1016/j.dsr.2014.10.006
700 Totsuka S, Shimada K, Nozaki T, Kimura J-I, Chang Q, Ishibashi J-i (2019) Pb isotope

compositions of galena in hydrothermal deposits obtained by drillings from active hydrothermal fields in the middle Okinawa Trough determined by LA-MC-ICP-MS. Chem Geol 514:90–104. https://doi.org/10.1016/j.chemgeo.2019.03.024

Tsuji T, Takai K, Oiwane H, Nakamura Y, Masaki Y, Kumagai H, Kinoshita M, Yamamoto F, Okano T, Kuramoto S (2012) Hydrothermal fluid flow system around the Iheya North Knoll in the mid-Okinawa trough based on seismic reflection data. J Volcanol Geotherm Res 213–214:41–50. https://doi.org/10.1016/j.jvolgeores.2011.11.007

Ueno H, Hamasaki H, Murakawa Y, Kitazono S, Takeda T (2003) Ore and gangue minerals of sulfide chimneys from the North Knoll, Iheya Ridge, Okinawa Trough, Japan. JAMSTEC Deepsea Res 22:49–62.

Yamamoto F, Maki T, Hyakudome T, Sawa T, Tsukioka S, Saito F, Ishikawa A, Chiba K (2009) High-resolution bathymetric and geological survey of the Iheya-north knoll, the Okinawa Trough, using AUV Urashima. Abstract of the 21st Meeting of the Japan Society for Marine Surveys and Technology P-07.

Yamamoto M, Nakamura R, Oguri K, Kawagucci S, Suzuki K, Hashimoto K, Takai K (2013) Generation of electricity and illumination by an environmental fuel cell in deep-sea hydrothermal vents. Angew Chem Int Ed 52(41):10758–10761. https://doi.org/10.1002/anie.201302704

Yamano M, Uyeda S, Kinoshita H, Hilde TWC (1986) Report on DELP 1984 cruises in the middle Okinawa Trough Part 4: heat flow measurements. Bull ERI Univ Tokyo 61:251–267.

Yamasaki T (2017) Petrography and whole-rock major and trace element analyses of igneous rocks from Iheya North Knoll, middle Okinawa Trough, SIP Expedition CK14-04 (Exp. 907). J Geol Soc Jpn 123(1):23–29. https://doi.org/10.5575/geosoc.2016.0049

Yamasaki T (2018) The role of bimodal magmatism in seafloor massive sulfide (SMS) ore-forming systems at the middle Okinawa Trough, Japan. Ocean Sci J 53(2):413–436. http://dx.doi.org/10.1007/s12601-018-0031-1

Yeats CJ, Hollis SP, Halfpenny A, Corona J-C, LaFlamme C, Southam G, Fiorentini M, Herrington RJ, Spratt J (2017) Actively forming Kuroko-type volcanic-hosted massive sulfide (VHMS) mineralization at Iheya North, Okinawa Trough, Japan. Ore Geol Rev 84:20–41. https://doi.org/10.1016/j.oregeorev.2016.12.014

FIGURE CAPTIONS

735 **Fig. 1** Maps of the Iheya-North hydrothermal field, middle Okinawa Trough, modified
736 from Kawagucci et al. (2013), Nakamura et al. (2015), and Nozaki et al. (*in press*).
737 Location maps show the regional setting of the Okinawa Trough and the Iheya-North
738 hydrothermal field (upper left), and the Original, Natsu, and Aki Sites in the Iheya-North
739 hydrothermal field (upper right). The locations of drilling sites during IODP Expedition
740 331 (Takai et al. 2011, 2012) and hydrothermal chimneys (Kawagucci et al. 2013) are
741 shown on the bathymetry around the Original Site (lower). Contour interval, 1 or 10 m.
742 The lower map is based on an echo sounder survey by AUV *Urashima* conducted during
743 cruise YK07-07 of R/V *Yokosuka* in May 2007 (Yamamoto et al. 2009). Abbreviations:
744 VAMP, volcanic arc migration phenomenon; ESBC, Ese South Big Chimney; HHH,
745 Hidden High-radioactivity Hill; HRV, High Radioactivity Vent; NBC, North Big
746 Chimney; NEC, North Edge Chimney; SBC, South Big Chimney.
747
748 **Fig. 2** ROV dive photos of the deep-sea artificial hydrothermal vent at Hole C0014G. (a,
749 b) Photos taken on 23 November 2013, 38 months after the drilling operation (dive
750 HPD#1598 of cruise NT13-23). (a) The vent pipe is clogged with scale, and many bubbles
751 are visibly rising into the seawater. (b) After this scale was removed with a hydraulic
752 chisel, vigorous hydrothermal fluid flow resumed; a flame structure is seen above the

753 steel vent pipe protruding above the corrosion cap on the guide base. (c, d) Photos taken
754 on 22 February 2016, 64 months after the initial drilling operation (cruise CK16-01, D/V
755 *Chikyu* Expedition 908). (c) The vent is completely clogged with scale. The scale sample
756 analyzed in this study was recovered at this time. (d) After scale removal, vigorous
757 discharge of hydrothermal fluid resumed once again. A flowmeter was installed to
758 measure the pressure, temperature, and flow rate of the hydrothermal fluid.
759
760 **Fig. 3** Photographs of the scale sample. (a) Top portion (sample no. C0014G 0–3 cm). (b)
761 A deeper portion (sample no. C0014G 3–8 cm) shows multiple concentric layers of dark
762 gray sphalerite with a semimetallic luster and thin layers of reddish-brown material. (c)
763 Enlarged image of a cross section through the top portion (sample no. C0014G 0–3 cm).
764 The red box indicates the area shown in photomicrographs (Figs. 4h and 4i). (d) Enlarged
765 image of a cross section through the deeper portion (sample no. C0014G 3–8 cm). The
766 red box indicates the area shown in photomicrographs (Figs. 4a–g).
767
768 **Fig. 4** Reflected-light photomicrographs of polished sections of the hydrothermal scale
769 sample. (a) Innermost part of sample C0014G 3–8 cm (pipe wall is on the left) showing,
770 from right to left, (1) a layer rich in dendritic galena with sphalerite (layer 1), (2) a layer

771 rich in botryoidal chalcopyrite (layer 2), (3) a layer rich in sphalerite with dendritic galena
772 (layer 3), and (4) a layer of coarse-grained sphalerite (layer 4). (b) Enlargement of layer
773 2 in Fig. 4a. (c) Enlargement of layers 2 and 3 in Fig. 4a. (d) Enlargement of layers 3 and
774 4 in Fig. 4a. (e) Porous reddish-brown material rich in galena and chalcopyrite (layer 5;
775 center) between layers of coarse-grained sphalerite (layer 4) in sample C0014G 3–8 cm.
776 The white box indicates the area enlarged in Fig. 4f. (f) Enlargement of the porous
777 reddish-brown material (layer 5) at the center of Fig. 4e. (g) Coarse-grained sphalerite in
778 sample C0014G 3–8 cm showing a crack filled with galena and chalcopyrite. (h)
779 Innermost part of sample C0014G 0–3 cm, in contact with ambient seawater, showing a
780 layer rich in barite (layer B). (i) Innermost part of sample C0014G 0–3 cm showing details
781 of the barite-rich layer (layer B) and dendritic sphalerite with galena.
782
783 **Fig. 5** Elemental Cu, Pb, Zn, Fe, S, and Ag maps of a polished surface of sample C0014G
784 3–8 cm. Thin rings, relatively bright in the Fe and Pb maps and dark in the Zn map,
785 correspond to the reddish-brown component; these rings are numbered in the Pb image.
786 Relatively high and low concentrations are shown by warm and cold colors, respectively.
787
788 **Fig. 6** Representative backscattered electron images of three zones in sample C0014G 8–

11 cm: (a) innermost zone of sphalerite with dendritic galena (layer 1 in Fig. 4a), (b) gray, coarse-grained (massive) sphalerite (layer 4 in Fig. 4d), and (c) reddish-brown sphalerite rich in galena and chalcopyrite (layer 5 in Figs. 4e and 4f). (d) Mn vs. Fe content diagram from measurements of nearly pure sphalerite (EPMA totals > 96 wt%, with <1 wt% Cu and Pb). The Fe content of sphalerite gradually decreases from zones (a) to (c) to (b) (layers 1, to 5, to 4). (e) Temperature vs. sulfur fugacity (log f_{S_2}) diagram for sphalerite. Fe contents (mole fraction) and fluid inclusion homogenization temperatures derived from sphalerite in zones (b) and (c) correspond to the precipitation conditions indicated by the red stars labeled *b* and *c*, respectively. Modified from Barton and Toulmin (1966) and Suzuki et al. (2008). Dashed contours, FeS content in sphalerite. Abbreviations: Ccp, chalcopyrite; Gn, galena; hf, hydrothermal fluid, Sp, sphalerite.

Fig. 7 (a, b) Representative backscattered electron images of cotunnite ($PbCl_2$) in sample C0014G 8–11 cm. Abbreviations: Ccp, chalcopyrite; Gn, galena; Sp, sphalerite.

Fig. 8 Photos of the polished sections of samples (a) C0014G 0–3 cm and (b) C0014G 20–23 cm used for fluid inclusion analyses. The analyses were limited to the three layers of coarse-grained sphalerite (layers I, II, and III, from interior to exterior) with low Fe

807 contents and, thus, sufficiently transparent crystals. Histograms of (c) homogenization
808 temperature (T_h, n = 35) and (d) salinity (wt% NaCl eq., n = 38) in sphalerite fluid
809 inclusions.
810
811 **Fig. 9** Elemental profiles of scale samples (bold red lines) and of sulfide- and sulfate-rich
812 portions of juvenile chimneys formed on other artificial hydrothermal vents (Nozaki et al.
813 2016), Kuroko-type VMS deposits on land (Ishibashi and Urabe 1995), Besshi-type VMS
814 deposits on land (Nozaki 2008), and chimneys on the East Pacific Rise (Fouquet et al.
815 1993). Values are normalized with respect to the average upper continental crust (UCC)
816 value (Taylor and McLennan 1985) and plotted at log scale.
817
818 **Fig. 10** Depth profiles for Fe, Cu, Zn, Sb, Ba, and Pb contents in the scale sample.
819
820 **Fig. 11** SEM images of sphalerite in sample C0014G 8–11 cm. (a, b) Tabular sphalerite
821 crystals are often covered by small (<5 μm) sphalerite grains. The tabular form consists
822 of {111} crystal faces, and the crystals are elongated in the ⟨110⟩ direction. (c) Void spaces
823 are often filled with small (<5 μm) sphalerite grains. These are also dominant near
824 boundaries between the reddish-brown and gray components. (d) Small (<5 μm)

825 sphalerite grains show distorted shapes with striated surfaces indicative of {111} twin
826 lamellae.
827
828 **Fig. 12** Conceptual diagrams of hydrothermal scale formation within the vent pipe. (a)
829 When the pipe is clogged by scale, isolation from the ambient seawater and subseafloor
830 boiling, confirmed by fluid inclusion analyses, produces hydrothermal fluid with low
831 sulfur fugacity (f_{S_2}) that results in sphalerite with a high Fe content and the precipitation
832 of the reddish-brown component rich in galena and chalcopyrite. (b) After scale removal,
833 the flow of hydrothermal fluid from the pipe becomes more vigorous and promotes local
834 entrainment of seawater beneath the seafloor, resulting in hydrothermal fluid with high
835 f_{S_2}, sphalerite with a low Fe content, and precipitation of dark, coarse-grained sphalerite.
836 Abbreviations: Ccp, chalcopyrite; Gn, galena; Sp, sphalerite.

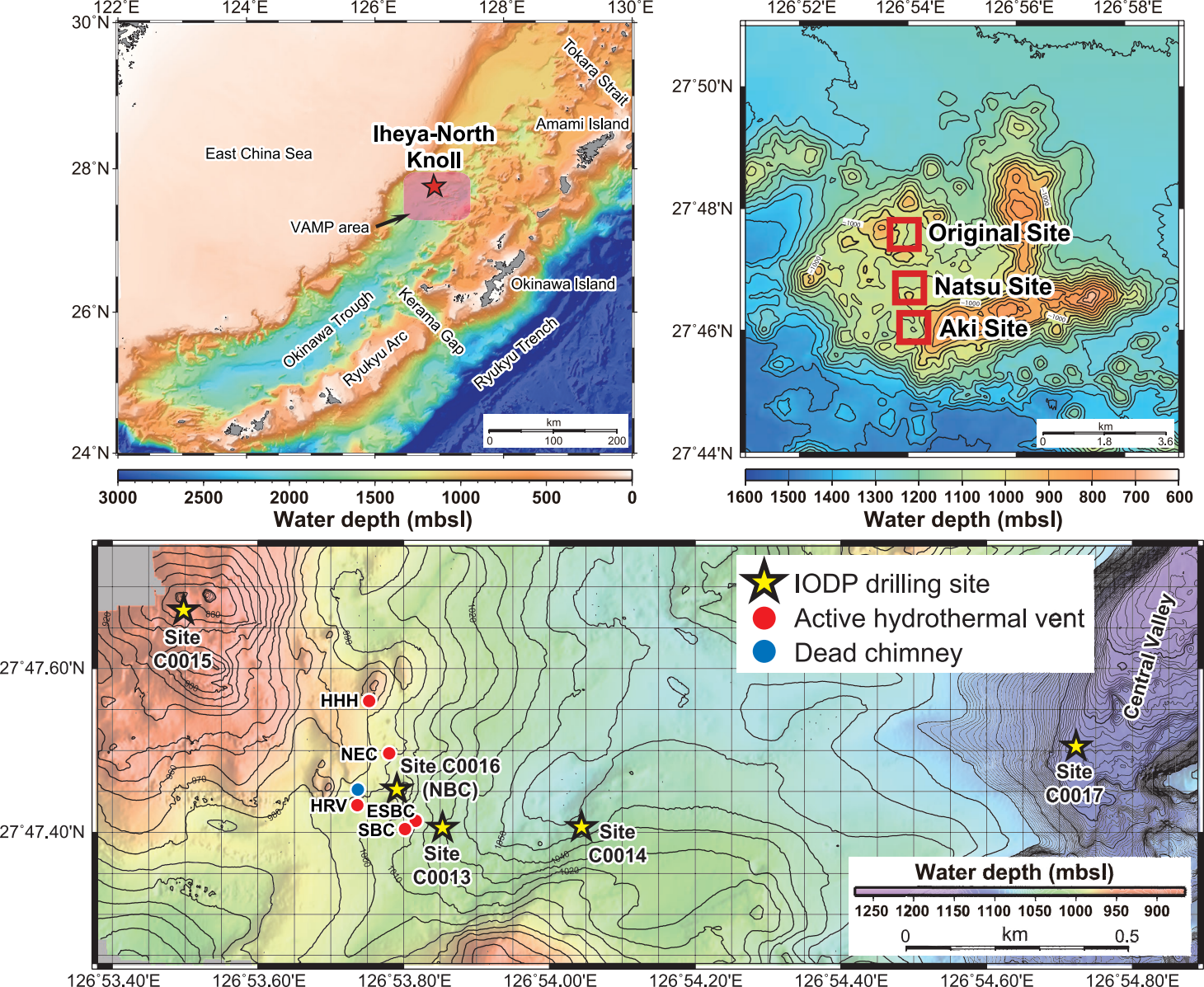
122°E
124°E
126°E
128°E
130°E
30°N
28°N
26°N
24°N
East China Sea
Iheya-North Knoll
Amami Island
Tokara Strait
VAMP area
Okinawa Island
Okinawa Trough
Kerama Gap
Ryukyu Arc
Ryukyu Trench
km
0
100
200
3000
2500
2000
1500
1000
500
0
Water depth (mbsl)
126°52'E
126°54'E
126°56'E
126°58'E
27°50'N
27°48'N
27°46'N
27°44'N
Original Site
Natsu Site
Aki Site
km
0
1.8
3.6
1600
1500
1400
1300
1200
1100
1000
900
800
700
600
Water depth (mbsl)
IODP drilling site
Active hydrothermal vent
Dead chimney
Site C0015
HHH
NEC
Site C0016 (NBC)
HRV
ESBC
SBC
Site C0013
Site C0014
Site C0017
Central Valley
27°47.60'N
27°47.40'N
Water depth (mbsl)
1250
1200
1150
1100
1050
1000
950
900
0
km
0.5
126°53.40'E
126°53.60'E
126°53.80'E
126°54.00'E
126°54.20'E
126°54.40'E
126°54.60'E
126°54.80'E

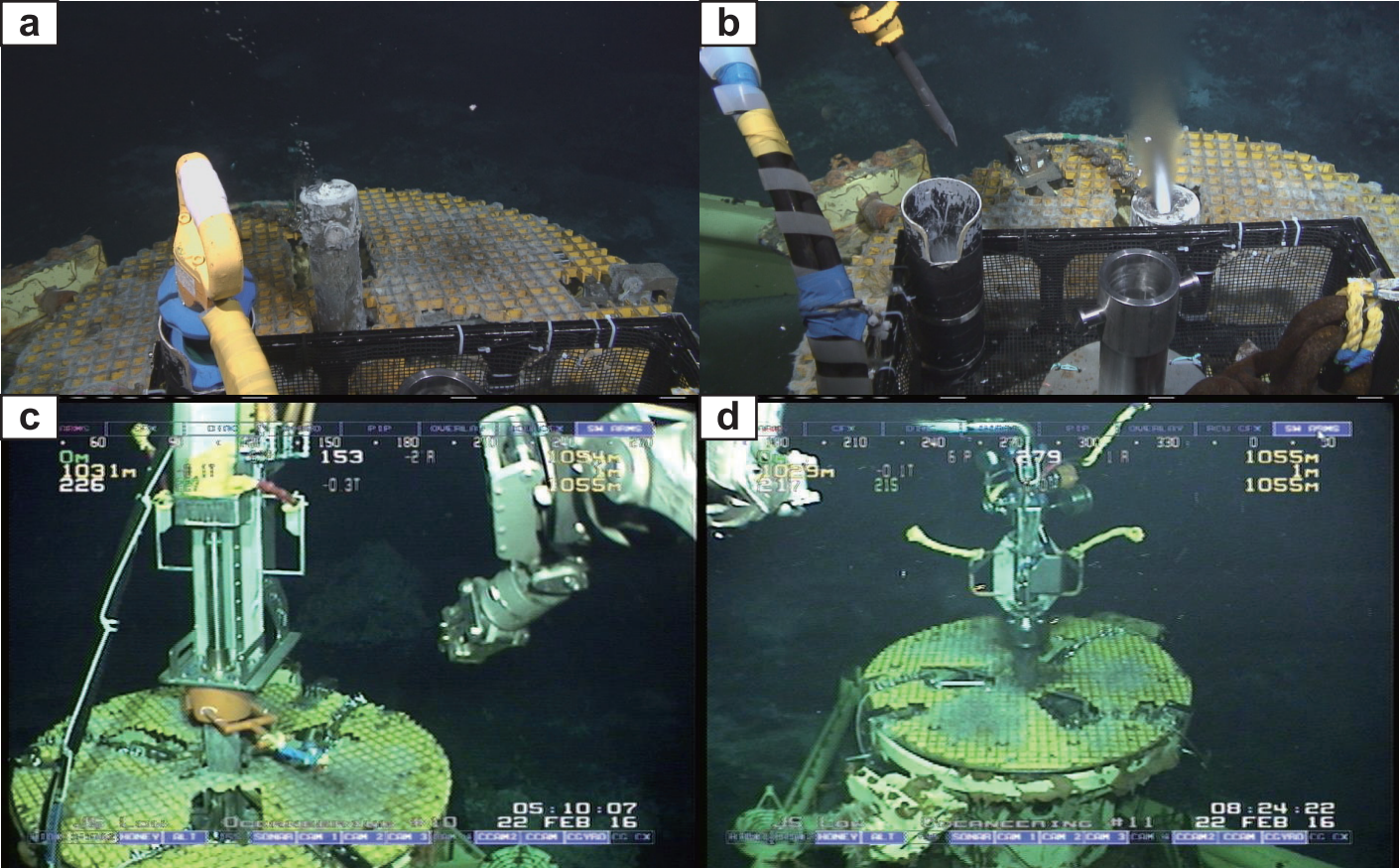
a
b
c
d
05:10:07
22 FEB 16
08:24:22
22 FEB 16

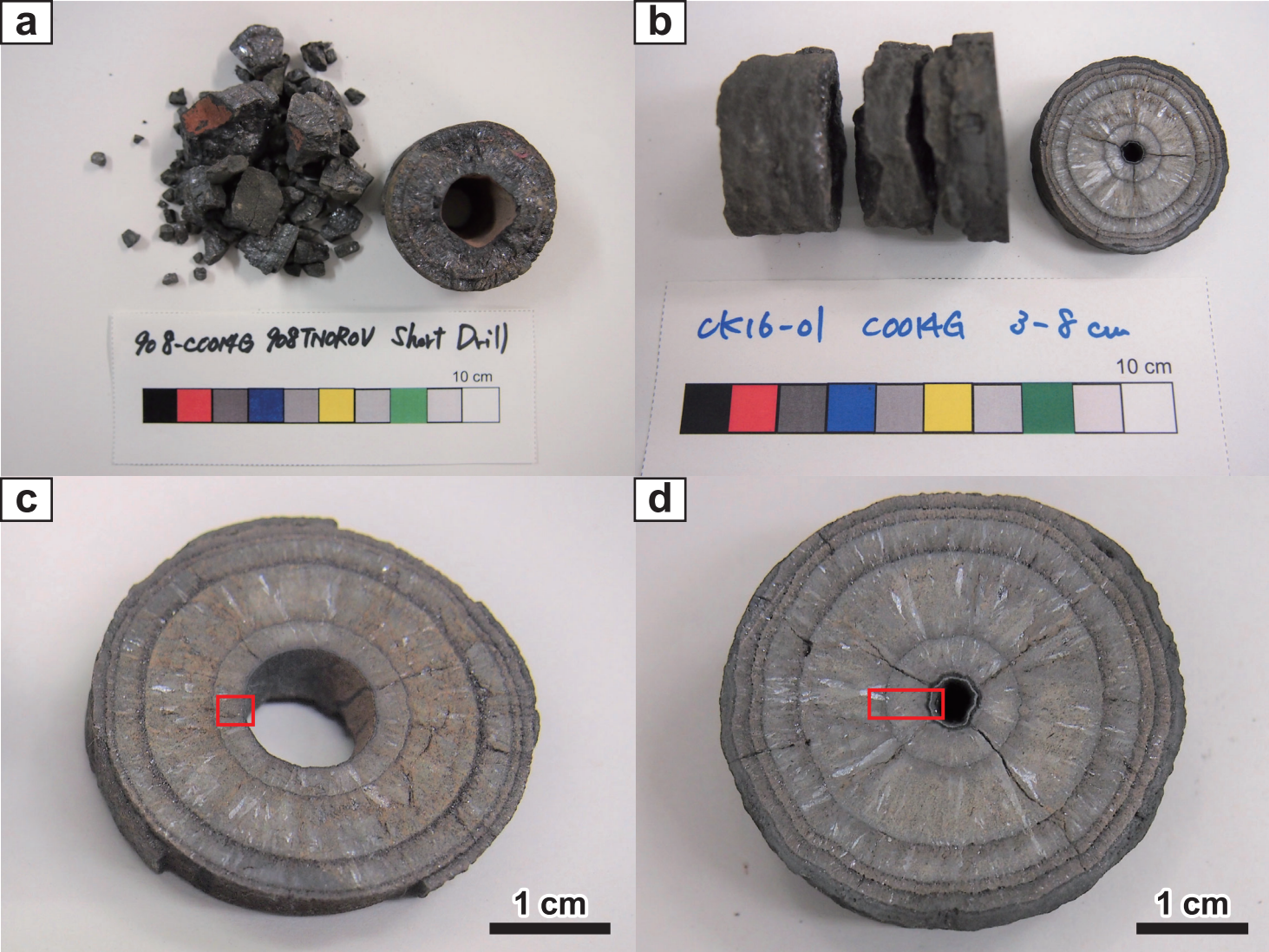
a
b
c
d
10 cm
10 cm
1 cm
1 cm

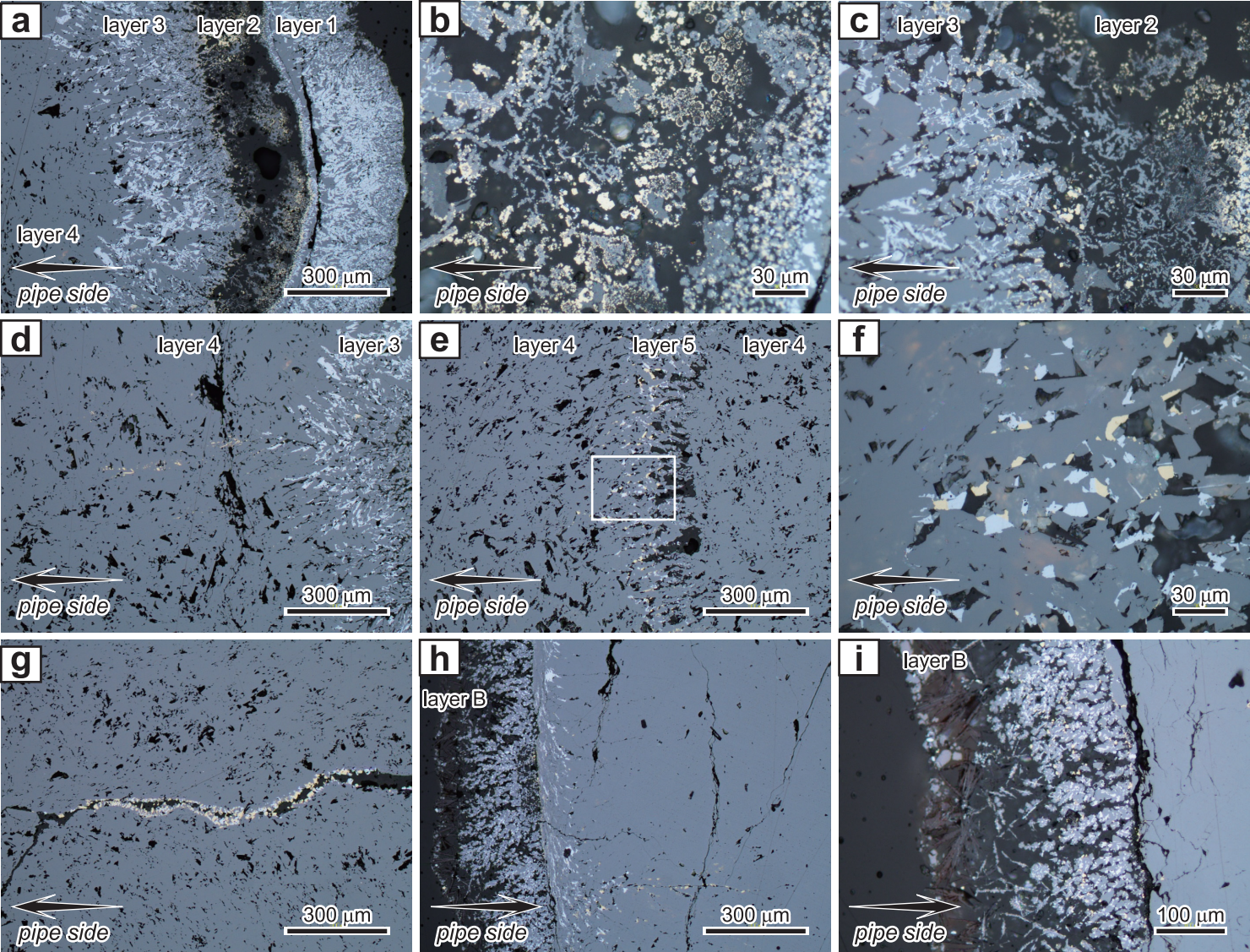
a
layer 3
layer 2
layer 1
layer 4
pipe side
300 µm
b
pipe side
30 µm
c
layer 3
layer 2
pipe side
30 µm
d
layer 4
layer 3
pipe side
300 µm
e
layer 4
layer 5
layer 4
pipe side
300 µm
f
pipe side
30 µm
g
pipe side
300 µm
h
layer B
pipe side
300 µm
i
layer B
pipe side
100 µm

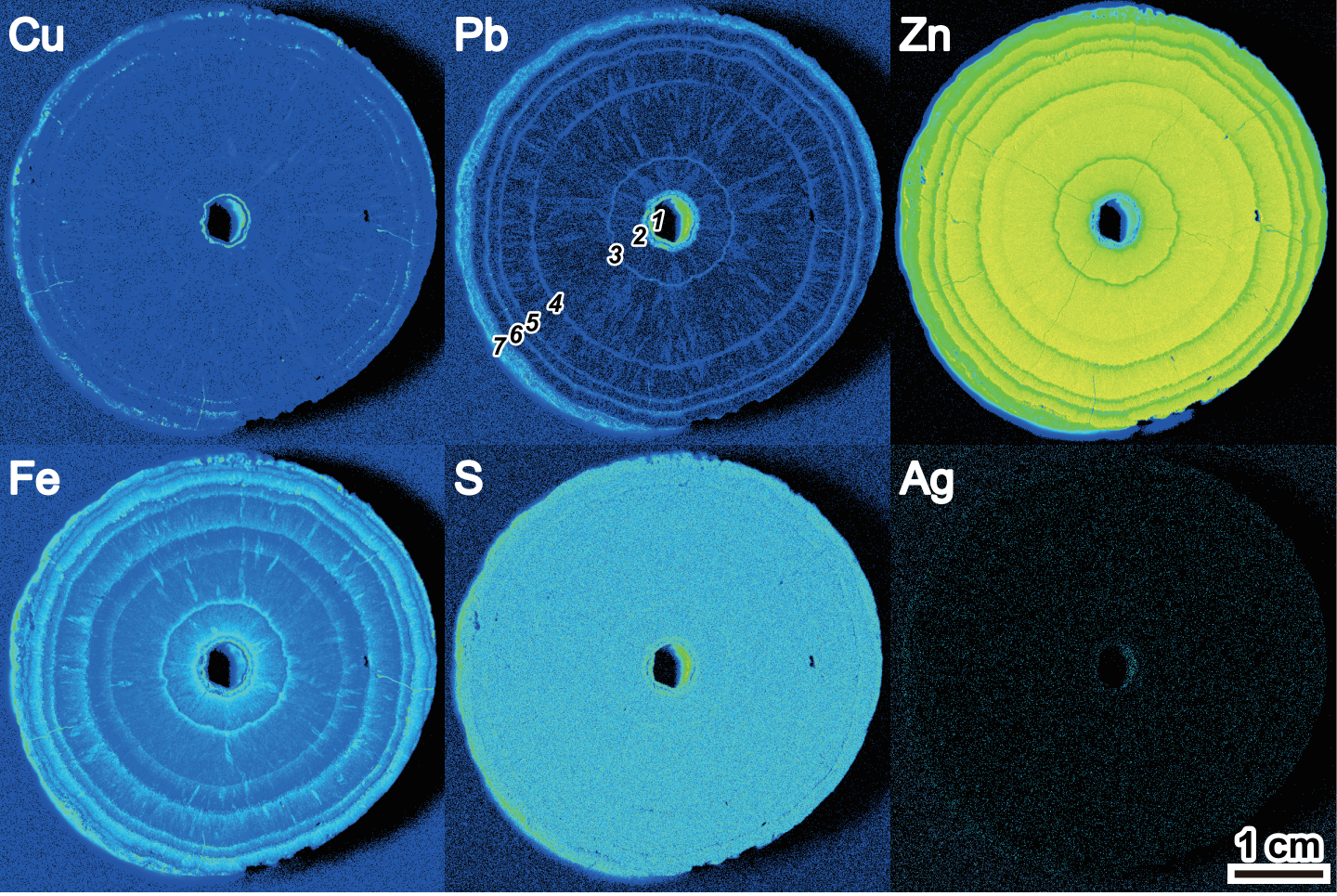
Cu
Pb
Zn
1
2
3
4
5
6
7
Fe
S
Ag
1 cm

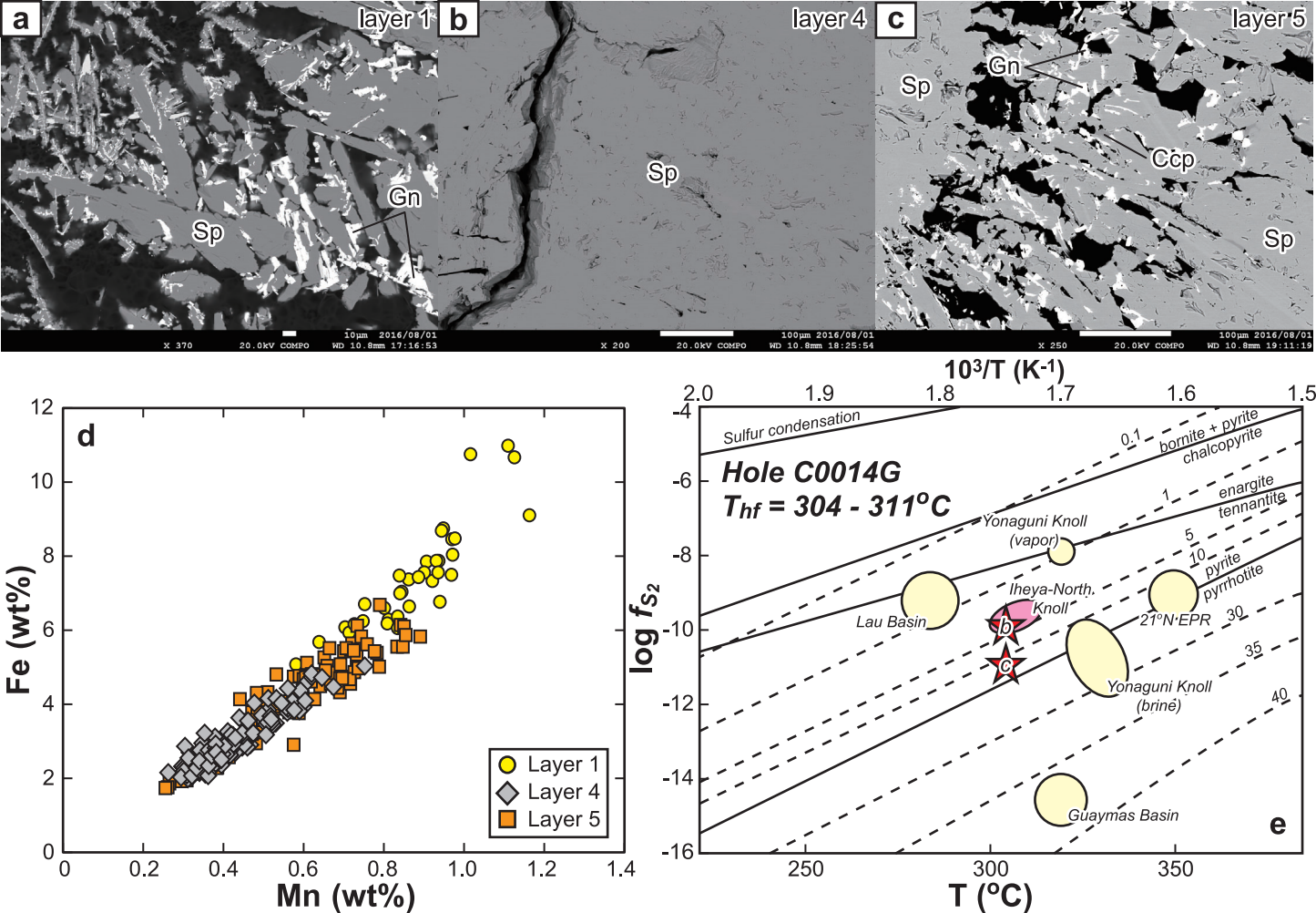
a
layer 1
Gn
Sp
b
layer 4
Sp
c
layer 5
Gn
Sp
Ccp
Sp
d
Fe (wt%)
Mn (wt%)
Layer 1
Layer 4
Layer 5
e
$10^3/T$ (K^{-1})
log f_{S_2}
T (°C)
Sulfur condensation
Hole C0014G
T_{hf} = 304 - 311°C
Yonaguni Knoll (vapor)
Iheya-North Knoll
Lau Basin
21°N·EPR
Yonaguni Knoll (brine)
Guaymas Basin
bornite + pyrite
chalcopyrite
enargite
tennantite
pyrite
pyrrhotite
0.1
1
5
10
30
35
40

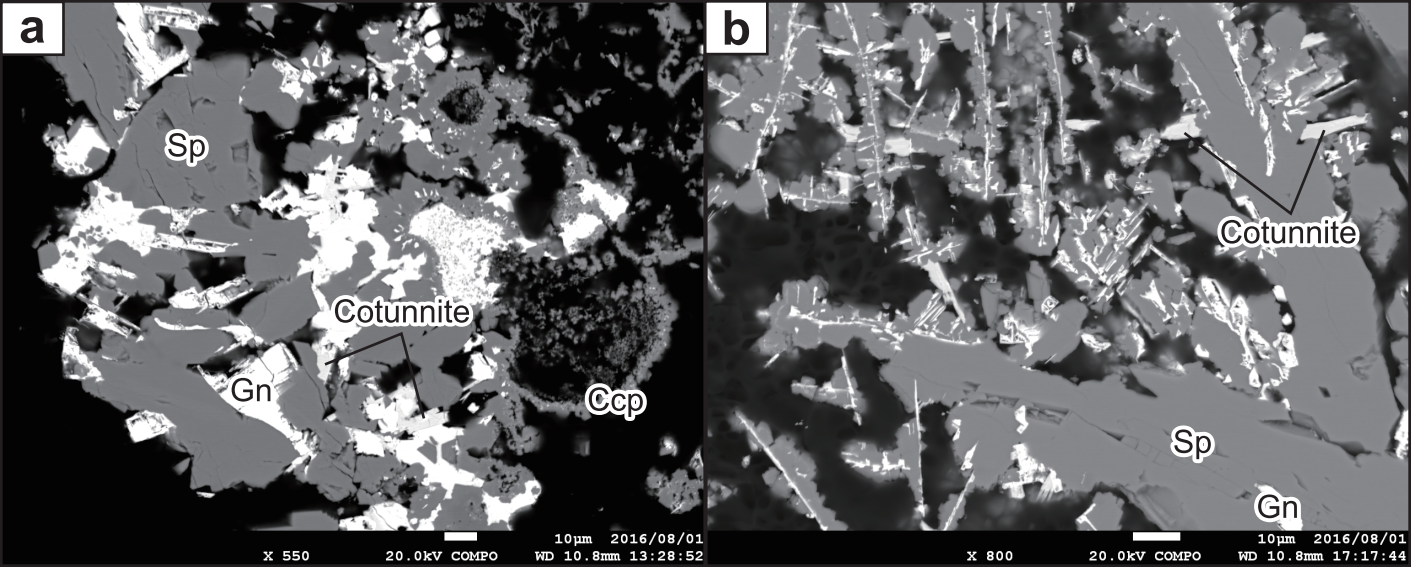
a
Sp
Cotunnite
Gn
Ccp
10μm 2016/08/01
X 550 20.0kV COMPO WD 10.8mm 13:28:52
b
Cotunnite
Sp
Gn
10μm 2016/08/01
X 800 20.0kV COMPO WD 10.8mm 17:17:44

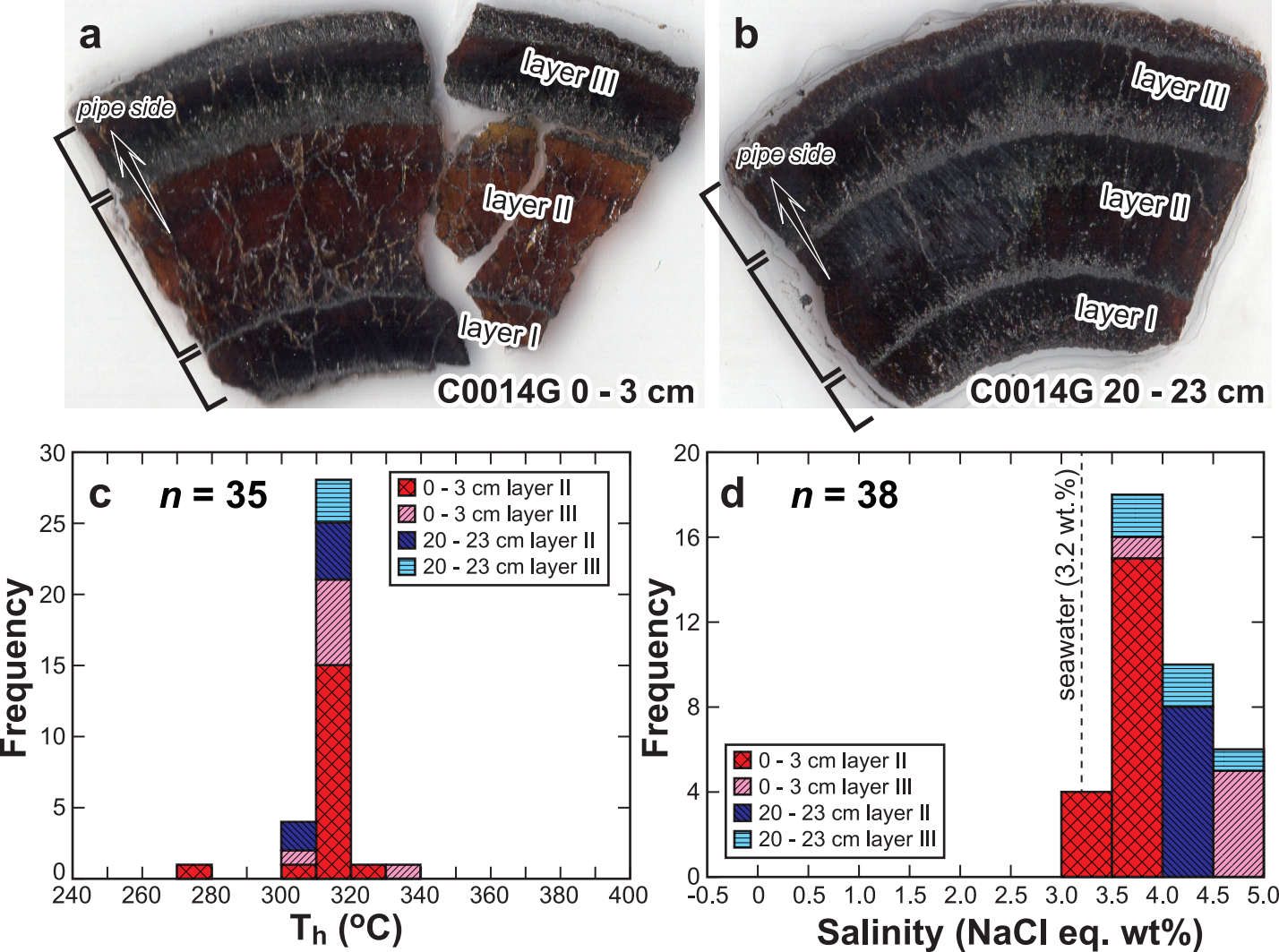
a
pipe side
layer III
layer II
layer I
C0014G 0 - 3 cm
b
pipe side
layer III
layer II
layer I
C0014G 20 - 23 cm
c
n = 35
0 - 3 cm layer II
0 - 3 cm layer III
20 - 23 cm layer II
20 - 23 cm layer III
Frequency
Th (ºC)
d
n = 38
seawater (3.2 wt.%)
Frequency
Salinity (NaCl eq. wt%)

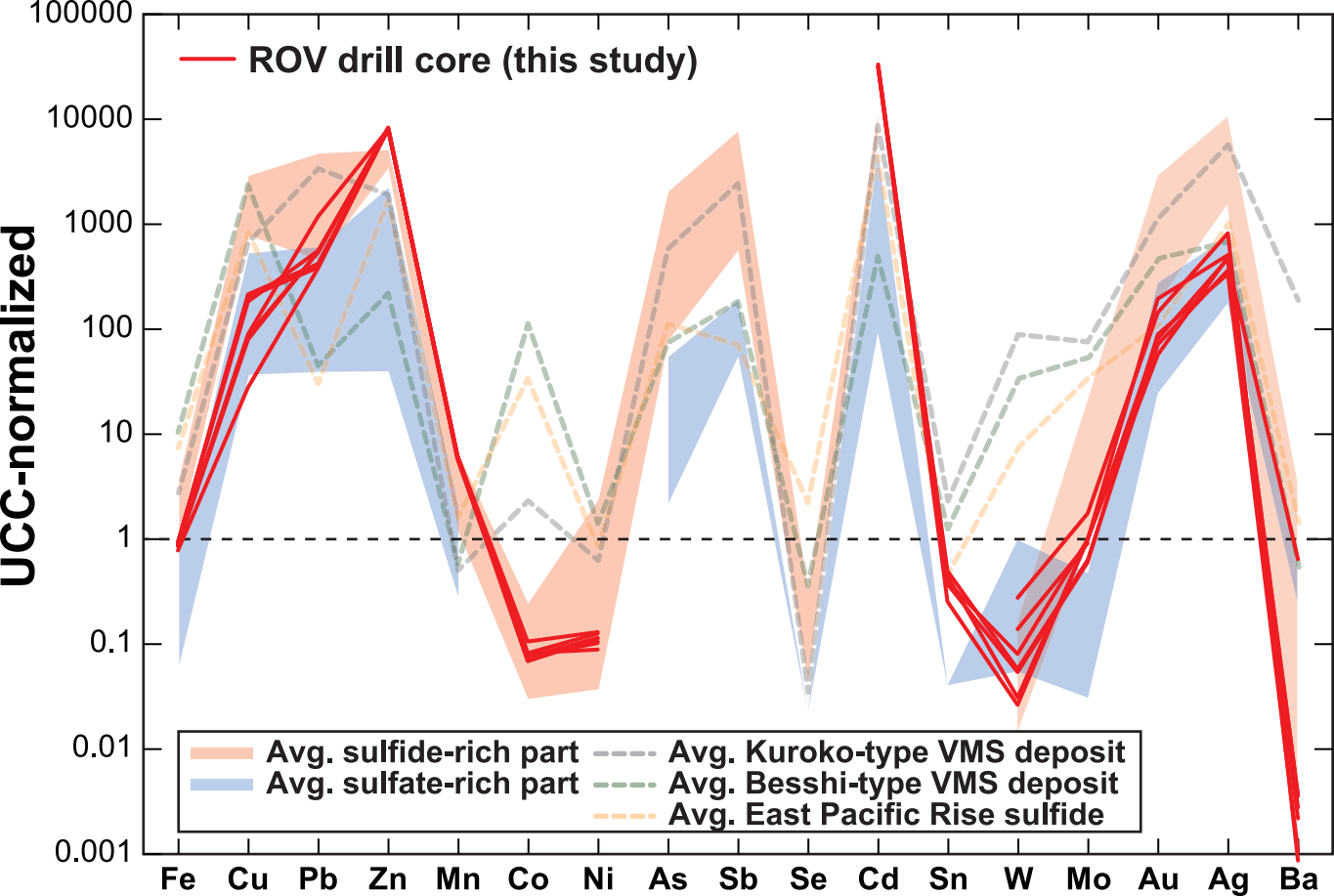
ROV drill core (this study)
UCC-normalized
100000
10000
1000
100
10
1
0.1
0.01
0.001
Fe
Cu
Pb
Zn
Mn
Co
Ni
As
Sb
Se
Cd
Sn
W
Mo
Au
Ag
Ba
Avg. sulfide-rich part
Avg. sulfate-rich part
Avg. Kuroko-type VMS deposit
Avg. Besshi-type VMS deposit
Avg. East Pacific Rise sulfide

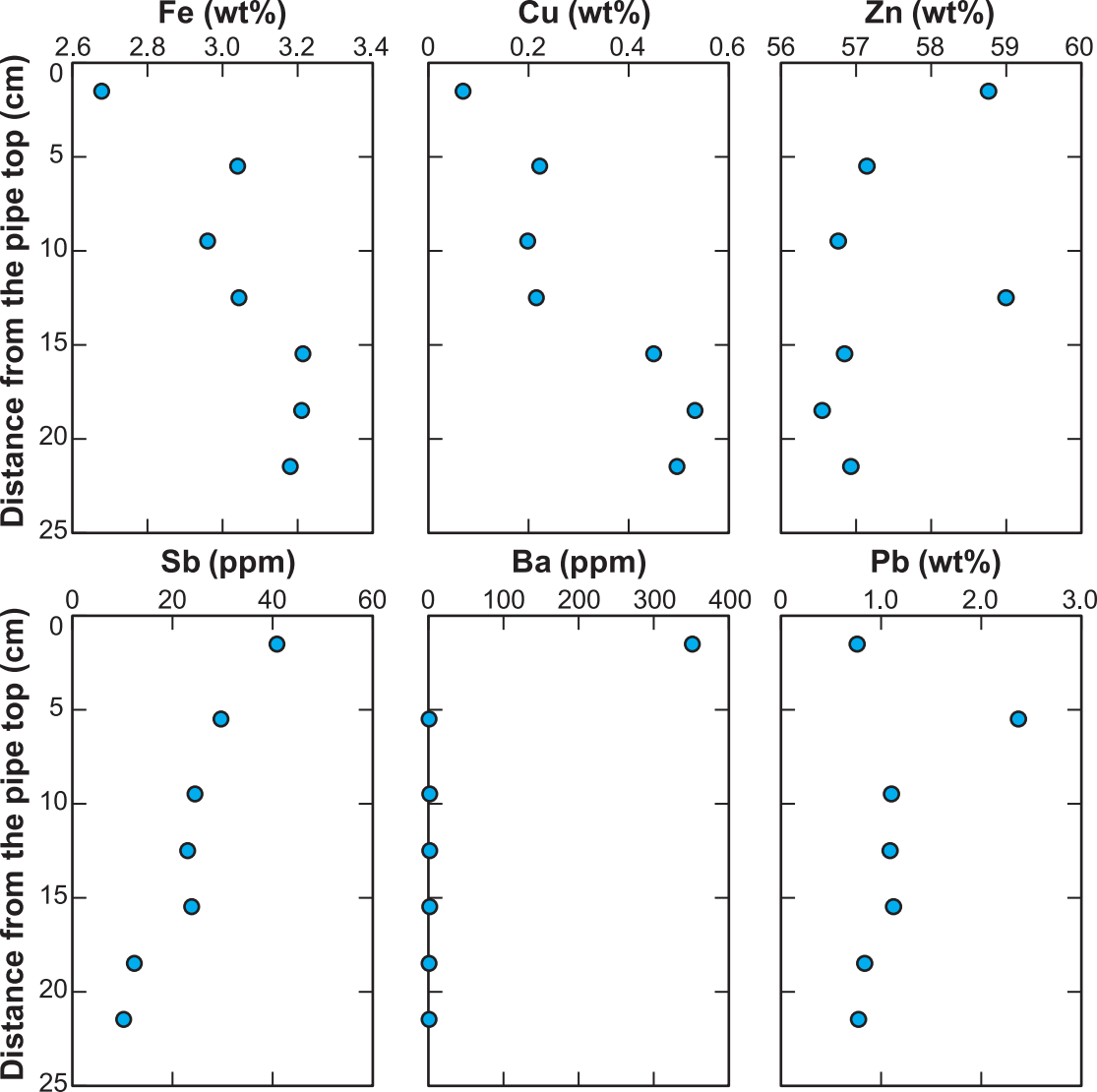
Fe (wt%)
2.6
2.8
3.0
3.2
3.4
Cu (wt%)
0
0.2
0.4
0.6
Zn (wt%)
56
57
58
59
60
Distance from the pipe top (cm)
0
5
10
15
20
25
Sb (ppm)
0
20
40
60
Ba (ppm)
0
100
200
300
400
Pb (wt%)
0
1.0
2.0
3.0

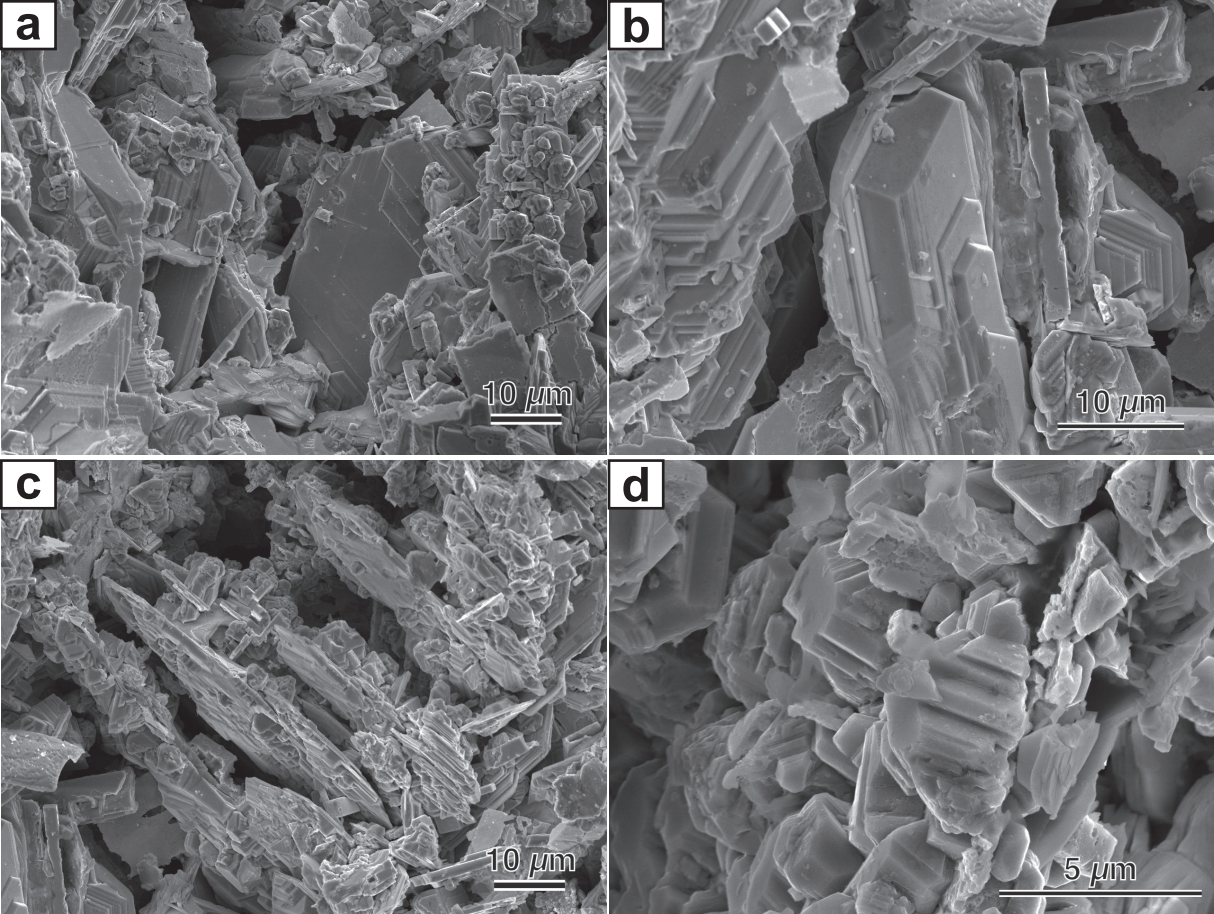
a
10 μm
b
10 μm
c
10 μm
d
5 μm

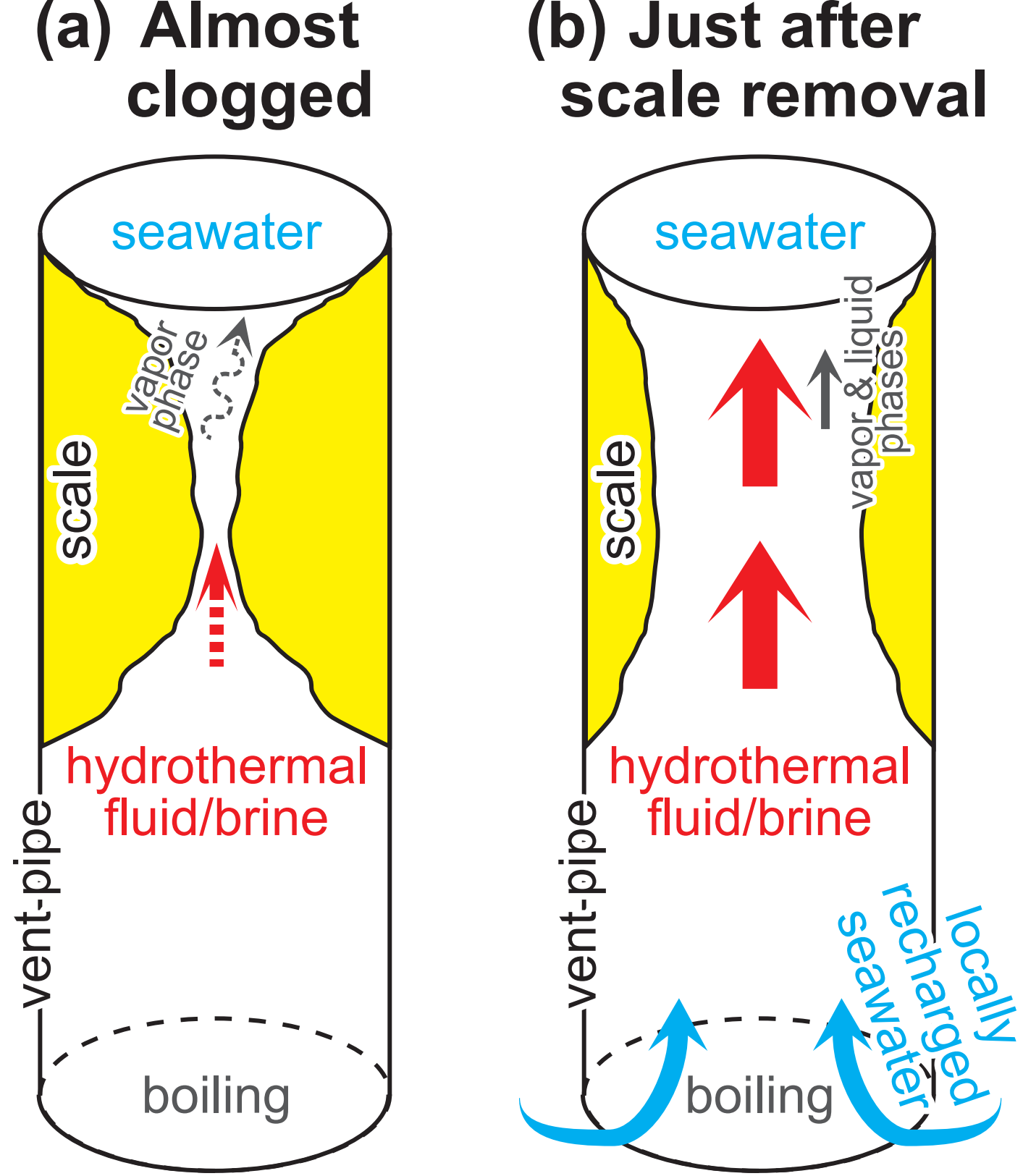

(1) Low fS_2
(2) High Fe in Sp
(3) Gn- and Cp-rich precipitation

(1) High fS_2
(2) Low Fe in Sp
(3) Coarse-grained Sp precipitation